A&A, 715, A102 (2026)
https://doi.org/10.1051/0004-6361/202661758
© The Authors 2026

Astronomy & Astrophysics

Dissecting the 3D chemo-dynamical structures of NGC 1381: A galaxy hosting an ancient slow bar with an accretion-related bulge and thick disc

Yunpeng Jin[1,⋆], Ling Zhu[2,⋆], Shude Mao[1], Marie Martig[3], Francesca Pinna[4,5], Glenn van de Ven[6], and Yuchen Ding[3]

[1] Department of Astronomy, Westlake University, Hangzhou, Zhejiang 310030, China
[2] Shanghai Astronomical Observatory, Chinese Academy of Sciences, 80 Nandan Road, Shanghai 200030, China
[3] Astrophysics Research Institute, Liverpool John Moores University, 146 Brownlow Hill, Liverpool L3 5RF, UK
[4] Instituto de Astrofísica de Canarias, calle Vía Láctea s/n, E-38205 La Laguna, Tenerife, Spain
[5] Departamento de Astrofísica, Universidad de La Laguna, Avenida Astrofísico Francisco Sánchez s/n, E-38206 La Laguna, Spain
[6] Department of Astrophysics, University of Vienna, Türkenschanzstraße 17, 1180 Wien, Austria

Received 1 July 2026 / Accepted 29 September 2026

ABSTRACT

We applied the barred population-orbit superposition method developed and validated in our previous 2025 papers to construct 3D chemo-dynamical models for the barred S0 galaxy NGC 1381 (FCC 170) in the Fornax cluster. Based on the properties of stellar orbits in the models, we decomposed NGC 1381 into six components with distinct kinematics and morphologies: (1) a dynamically warm nuclear disc; (2) a rigidly rotating, boxy, peanut, or X-shaped bar; (3) a dynamically hot, spheroidal bulge; (4) a dynamically cold thin disc; (5) a vertically extended thick disc with slightly slower rotation than the thin disc; and (6) a dynamically hot, spatially diffuse stellar halo. The luminosity fractions of the dynamical components indicate that the luminosity of NGC 1381 is dominated by the bar ($f_{\rm bar} \sim 30\%$) and thin disc ($f_{\rm thin} \sim 28\%$), with notable contributions from the thick disc ($f_{\rm thick} \sim 16\%$) and bulge ($f_{\rm bulge} \sim 17\%$) and only minor contributions from the nuclear disc ($f_{\rm nucl} \sim 5\%$) and halo ($f_{\rm halo} \sim 5\%$). The nuclear disc, bar, and thin disc are metal-rich ($[Z/H] \gtrsim 0$), α-poor ($[Mg/Fe] \lesssim 0.2$), and old (~13 Gyr), consistent with in situ formation in the early Universe. The bulge, thick disc, and stellar halo are metal-poor ($[Z/H] \lesssim 0$), α-rich ($[Mg/Fe] \gtrsim 0.2$), and younger than or comparable in age to the in situ components, suggesting that they are related to ex situ formation through the accretion of minor mergers. Further analysis of stellar population gradients for these ex situ-related components reveals that the thick disc and stellar halo, with their flat metallicity and [Mg/Fe] gradients, are likely dominated by a similar ex situ population. In contrast, the bulge exhibits a negative metallicity gradient ($\nabla[Z/H]_{\rm bulge} < 0$), which might originate from either predominantly ex situ stars or a mixture of in situ and ex situ stars; the bulge's ex situ fraction cannot be quantified with the current data. Our modelling also reveals the presence of a slow bar ($\mathcal{R} = 2.40^{+0.54}_{-0.27}$), with a bar pattern speed of $\Omega_p = 34^{+4}_{-7}\,{\rm km\,s^{-1}\,kpc^{-1}}$, a bar length of $R_{\rm bar} = 2.24^{+0.43}_{-0.22}$ kpc, and a corotation radius of $R_{\rm CR} = 5.38^{+1.59}_{-0.28}$ kpc, which is consistent with its ancient formation time.

Key words. galaxies: fundamental parameters – galaxies: individual: NGC 1381 – galaxies: kinematics and dynamics – galaxies: structure

1. Introduction

The classifications of galaxy structures originated from their morphologies and colours. For instance, the central regions of galaxies were initially classified as either red, spheroidal 'classical bulges' or blue, flat 'pseudobulges' linked to secular evolution (e.g. Kormendy & Kennicutt 2004; Athanassoula 2005). However, later detailed morphological analyses have revealed the complexity of bulge regions (e.g. Buta et al. 2015). Recent observations have uncovered composite bulges in some galaxies, where distinct structures such as a classical bulge, a bar, and a nuclear disc can coexist (e.g. Erwin et al. 2021; Tahmasebzadeh et al. 2024).

In standard models of galaxy formation, bars, nuclear discs, and classical bulges have distinct origins: bars can form through internal instabilities in rotation-dominated discs (e.g. Hohl 1971; Ostriker & Peebles 1973; Efstathiou et al. 1982) or external tidal perturbations (e.g. Noguchi 1996; Łokas 2018; Yoon et al. 2019); nuclear discs assemble from gas inflow towards galaxies' centres channelled by bars (e.g. Athanassoula 2003; Kormendy & Kennicutt 2004; Gadotti 2011); and classical bulges likely originate from dissipationless collapse or mergers (e.g. Bournaud et al. 2007; Fisher & Drory 2008; Gadotti 2009; Hopkins et al. 2010). However, how these formation mechanisms collectively influence the assembly history of galaxies, including the roles of in situ star formation and external accretion, remains poorly understood.

A key to understanding different structures lies in decomposing them using line-of-sight information. The traditional photometric decomposition techniques have been widely used over the past few decades. These techniques rely on strong assumptions such as bulges described by Sersic (1968) profiles, discs modelled by exponential profiles, and bars approximated as

⋆ Corresponding authors: jyp199333@163.com; lzhu@shao.ac.cn

Open Access article, published by EDP Sciences, under the terms of the Creative Commons Attribution License (https://creativecommons.org/licenses/by/4.0), which permits unrestricted use, distribution, and reproduction in any medium, provided the original work is properly cited.
This article is published in open access under the Subscribe to Open model. Subscribe to A&A to support open access publication.

prolate Ferrers bars (see Binney & Tremaine 2008). However, these assumptions often deviate from reality. Previous studies have shown that the surface brightness profiles of discs can be down-bending or up-bending in their inner or outer regions (e.g. Méndez-Abreu et al. 2017; Breda et al. 2020; Ding et al. 2023), while real bars can be triaxial, exhibiting boxy, peanut, or X-shaped (hereafter BP/X-shaped) structures (e.g. Shaw 1987; Lütticke et al. 2000; Erwin & Debattista 2017; Li et al. 2017). A recent study by Gadotti (2026) demonstrated that whether photometrically decomposed bulges are identified as classical bulges or nuclear discs depends on both the optimisation algorithms used and the imaging data quality. All these findings indicate that traditional photometric decomposition techniques struggle to reliably distinguish between structures of different physical origins.

Compared to traditional photometric decomposition, dynamical decomposition can better trace the physical origins of different galaxy structures, as demonstrated in cosmological simulations (e.g. Du et al. 2019, 2020; Pulsoni et al. 2020; Ortega-Martinez et al. 2022; Zana et al. 2022; Cristiani et al. 2024). In recent years, multiple integral field spectroscopy (IFS) surveys (e.g. Bacon et al. 2001, 2017; Cappellari et al. 2011; Sánchez et al. 2012; Bryant et al. 2015; Bundy et al. 2015) have delivered spatially resolved spectra for thousands of nearby galaxies. From these spectra, one can derive stellar kinematic and population maps, enabling both the dynamical decomposition of real galaxies and the subsequent analysis of their chemical properties.

The dynamical decomposition of real galaxies can be performed using Schwarzschild's orbit-superposition method (Schwarzschild 1979, 1982, 1993), in which 3D galaxy models are constructed via fitting of the luminosity distributions and stellar kinematic maps. This method has multiple implementations (e.g. van den Bosch et al. 2008; Long & Mao 2018; Vasiliev & Valluri 2020; Neureiter et al. 2021; Quenneville et al. 2022; Dattathri et al. 2024). The triaxial implementation developed by van den Bosch et al. (2008) (see also the publicly available version DYNAMITE[1]; Jethwa et al. 2020) was initially designed without accounting for bars. It has been validated in simulations (e.g. Zhu et al. 2018a; Jin et al. 2019) and has been used to analyse dynamical structures of galaxies in IFS surveys (e.g. Zhu et al. 2018a,b,c; Jin et al. 2020; Santucci et al. 2022, 2023; Thater et al. 2025). Subsequently, this implementation was updated to support the modelling of stellar populations (e.g. Poci et al. 2019, 2021; Zhu et al. 2020, 2022a,b; Ding et al. 2023; Jin et al. 2024) and to include bar structures for non-edge-on cases (inclination angle $\theta \lesssim 80°$; Tahmasebzadeh et al. 2021, 2022, 2024). The combination of dynamical modelling with stellar populations enables a powerful way to uncover the assembly history of galaxies (van de Ven et al. 2025). In recent work (Jin et al. 2025a,b), we further enhanced this method by simultaneously incorporating bars and stellar populations in the modelling and extending it to handle edge-on ($\theta \gtrsim 80°$) galaxies. This improved method was validated using simulated galaxies from the Auriga simulations (Grand et al. 2017, 2024) and can estimate the bar pattern speeds with a relative uncertainty of $\lesssim$15% for both side-on and end-on bars (Jin et al. 2025a). This method can also reliably characterise the luminosity distributions, ages, and metallicities of various dynamical structures, including bars, bulges, discs, and stellar halos (Jin et al. 2025b).

NGC 1381 (FCC 170) is an edge-on disc galaxy located in the central dense region of the Fornax cluster, with an estimated stellar mass of $2.25 \times 10^{10}\,M_\odot$ (Iodice et al. 2019a) and a distance of 19.57 Mpc (Spriggs et al. 2021; see also Blakeslee et al. 2009 for a slightly different value). This galaxy was classified as an S0 galaxy (Ferguson 1989). Subsequently, both optical and near-infrared images (e.g. Lütticke et al. 2000; Bureau et al. 2006; Venhola et al. 2018) revealed an obvious boxy bulge in its central region, which indicates the possible existence of a bar. The stellar kinematic maps confirm the presence of a bar by presenting an anti-correlated, correlated, and anti-correlated again h_3–V relation along the galaxy's major axis (Fig. 2; see also Pinna et al. 2019a; Poci et al. 2021). The positive h_3–V correlation is recognised as a robust bar diagnostic (e.g. Bureau & Athanassoula 2005; Molaeinezhad et al. 2016; Li et al. 2018), while the negative h_3–V correlation at the innermost regions is the signature of a bar-induced nuclear disc (e.g. Chung & Bureau 2004; Bureau & Athanassoula 2005; Gadotti et al. 2020; Fraser-McKelvie et al. 2025). This galaxy likely fell into the Fornax cluster approximately 8–12 Gyr ago (e.g. Iodice et al. 2019b; Ding et al. 2023). During the galaxy's infall, interactions with the intracluster medium stripped the hot ionised gas from its stellar halo, cutting off the gas supply for star formation and resulting in strangulation-dominated quenching (e.g. Morokuma-Matsui et al. 2022; Martig et al. 2026) and, consequently, old stellar populations in the BP/X-shaped regions nowadays (e.g. Pinna et al. 2019a; Martín-Navarro et al. 2021). This implies that NGC 1381 probably formed its bar in the early Universe before falling into the cluster, with its internal structures preserved as fossil records until the present day.

The structures of NGC 1381 have been studied in previous works, but the different components in the galaxy's inner regions were not accurately distinguished. For example, based directly on the projected 2D morphology, kinematics, and stellar populations, Pinna et al. (2019a) divided the galaxy into distinct regions, each dominated by a different structure: a nuclear disc, a boxy structure, a thin disc, and inner and outer thick discs. Dynamical decompositions based on orbit-superposition modelling were later performed by Poci et al. (2021) and Ding et al. (2023); however, their models did not explicitly include a non-axisymmetric bar and did not concentrate much on the nuclear disc. In this work, we modelled NGC 1381 using the barred population-orbit superposition method (Jin et al. 2025a,b), which can effectively disentangle the bar and the dynamically hot bulge. This enabled a full dynamical decomposition of the galaxy into a nuclear disc, a bar, a bulge, a thin disc, a thick disc, and a stellar halo. We derived the 3D spatial distributions, kinematics, and chemical properties of these components, including the bar pattern speed and bar length.

The paper is organised as follows. In Sect. 2, we introduce the photometric and spectroscopic data we used. In Sect. 3, we describe how we constructed barred population-orbit superposition models for NGC 1381, including the stellar-orbit-based dynamical decomposition. In Sect. 4, we characterise the bar, including its pattern speed, length, and corotation radius, as well as the luminosity distributions and chemical properties of all decomposed components. We discuss our results in Sect. 5 and summarise our conclusions in Sect. 6.

Throughout the paper, the coordinate system (x', y') represents the observing plane, with the galaxy's major axis aligned with the x'-axis. The intrinsic bar's rotating frame is denoted as (x, y, z), where the x-axis and y-axis coincide with the bar's major and minor axes, respectively. The inertial frame (x_0, y_0, z) coincides with (x, y, z) at the initial time but deviates from it at later times due to the figure rotation about the z-axis.

[1] https://dynamics.univie.ac.at/dynamite_docs/

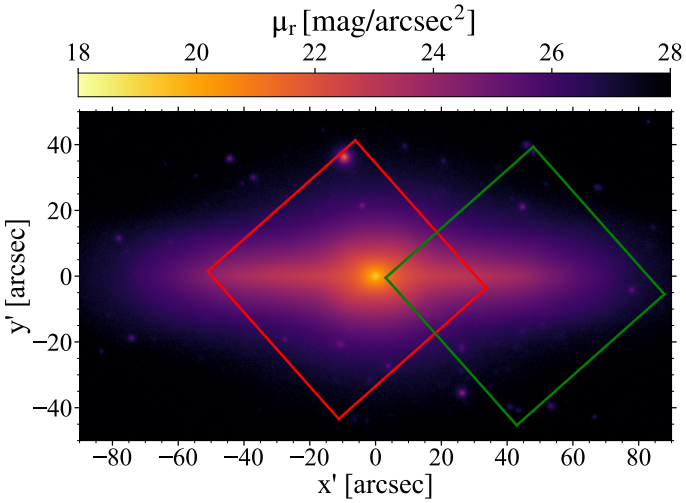


Fig. 1. Imaging and MUSE coverage of NGC 1381 (FCC 170). The image shows the deep r-band imaging from FDS, with its major axis rotated to the x'-axis and its surface brightness indicated by the colour bar. The red and green squares represent the central and halo MUSE pointings from F3D, respectively.

2. Photometric and spectroscopic data

2.1. The Fornax deep survey and the Fornax3D project

The Fornax Deep Survey (FDS; Iodice et al. 2016) is a deep multiband optical imaging survey covering the entire Fornax cluster out to the virial radius (~0.7 Mpc; Drinkwater et al. 2001). The observations were conducted using the 2.6-meter Very Large Telescope (VLT) Survey Telescope located at Cerro Paranal, Chile. We used the r-band deep imaging from FDS, which reaches a surface brightness level of ~27 mag arcsec^{-2} (Venhola et al. 2018).

The Fornax3D project (F3D; Sarzi et al. 2018) is an IFS survey targeting the 33 brightest galaxies within or near the virial radius of the Fornax cluster (Ferguson 1989). The observations were conducted using the wide-field mode of the Multi-Unit Spectroscopic Explorer (MUSE) instrument on the VLT (Bacon et al. 2010). MUSE provides a field of view of 1 × 1 arcmin^2 with a spatial sampling of 0.2 × 0.2 arcsec^2. The wavelength coverage is 4650–9300 Å with a spectral resolution of 2.5 Å (full width at half maximum) at 7000 Å. NGC 1381 is one of the 33 target galaxies and was observed with two MUSE pointings. Fig. 1 displays its r-band image and the regions covered by MUSE.

2.2. Stellar kinematics and populations

The stellar kinematic maps we adopted were derived following the same approach as Iodice et al. (2019b) but with an improved signal-to-noise ratio (S/N) of 100. These maps were generated by applying the full spectral fitting software pPXF (Cappellari & Emsellem 2004; Cappellari 2017) to spectra binned with the Voronoi 2D method (Cappellari & Copin 2003). The maps include the mean velocity (V), velocity dispersion (σ), higher-order velocity moments parametrised by the Gauss-Hermite coefficients (h_3 and h_4; Gerhard 1993; van der Marel & Franx 1993; Rix et al. 1997), and their corresponding errors. Since our dynamical modelling is triaxial, we further point-symmetrised the kinematic maps and their error maps to reduce noise and presented them in Fig. 2.

We employed three versions of stellar population maps: Version A originates from Martig et al. (2026), using Voronoi-binned spectra with $S/N = 60$; version B is based on Pinna et al. (2019a) but with S/N improved to 100 ($S/N = 40$ in the original work); version C is from Martín-Navarro et al. (2021), also with $S/N = 100$. All versions were derived by applying the pPXF fitting to Voronoi-binned spectra, with stellar population synthesis models (Vazdekis et al. 2010, 2015) based on the MILES stellar libraries (Sánchez-Blázquez et al. 2006) and BaSTI isochrones (Pietrinferni et al. 2004, 2006). Versions A and B are mass-weighted and assume a constant Kroupa (2001) initial mass function (IMF), using spectra covering 4750–5500 Å and a fixed regularisation parameter of 0.05, with the spatial coverage of the maps similar to that of the kinematic maps. In contrast, version C is light-weighted, allows for the variation in the IMF, and uses spectra covering 4800–6400 Å. Version C has a smaller spatial coverage because pixels with $S/N < 5$ were not included during the Voronoi-binning process. Compared to versions A and B, version C has an offset of ~−0.3 dex in metallicity and ~0.05 dex in [Mg/Fe] abundance due to different settings when fitting the spectra, but the spatial trends in the maps are similar.

Figure 2 shows the maps of stellar age, metallicity, and [Mg/Fe] abundance for version A, with their error maps derived from the Monte Carlo simulations of perturbed spectra. The stellar population maps for versions B and C are presented in the left panels of Figs. A.1 and A.2, respectively. Versions B and C did not include error maps, and we thus adopted fixed uncertainties of 1 Gyr for age, ~0.05 dex for metallicity, and ~0.03 dex for [Mg/Fe] abundance. These uncertainties generally agree with those of version A, as well as with estimates from previous studies of NGC 1381 and other galaxies with similar MUSE data (e.g. Pinna et al. 2019a,b; Martig et al. 2021; Sattler et al. 2023, 2025). We treated data version A as the default version in our analysis. It will be shown later that the fixed uncertainties in versions B and C do not affect our main findings.

3. Constructing barred population-orbit superposition models

We constructed the barred population-orbit superposition models in three major steps. First, we built barred orbit-superposition models by simultaneously fitting the stellar luminosity distributions and kinematic data (Sect. 3.1). Then, we categorised the stellar orbits in our models into different dynamical structures based on their orbital properties (Sect. 3.2). Finally, we assigned ages and metallicities to the orbits by fitting the stellar age and metallicity maps (Sect. 3.3). Our methodology for the first step follows Jin et al. (2025a), but has been modified to include a supermassive black hole. For the second and third steps, it follows Jin et al. (2025b), with updated orbit classification criteria during the decomposition. The model uncertainties we adopted throughout the paper are introduced in Sect. 3.4.

3.1. Constructing barred orbit-superposition models

To construct a barred orbit-superposition model, the gravitational potential is first built from four components: (1) a triaxial stellar bar with constant figure rotation, Ω_p; (2) an axisymmetric stellar disc aligned with the bar's major axis; (3) a spherical dark matter halo; and (4) a central supermassive black hole.

The stellar potential calculation begins with fitting the galaxy's surface brightness (r-band deep imaging from FDS) using the multi-Gaussian expansion (MGE) formal-

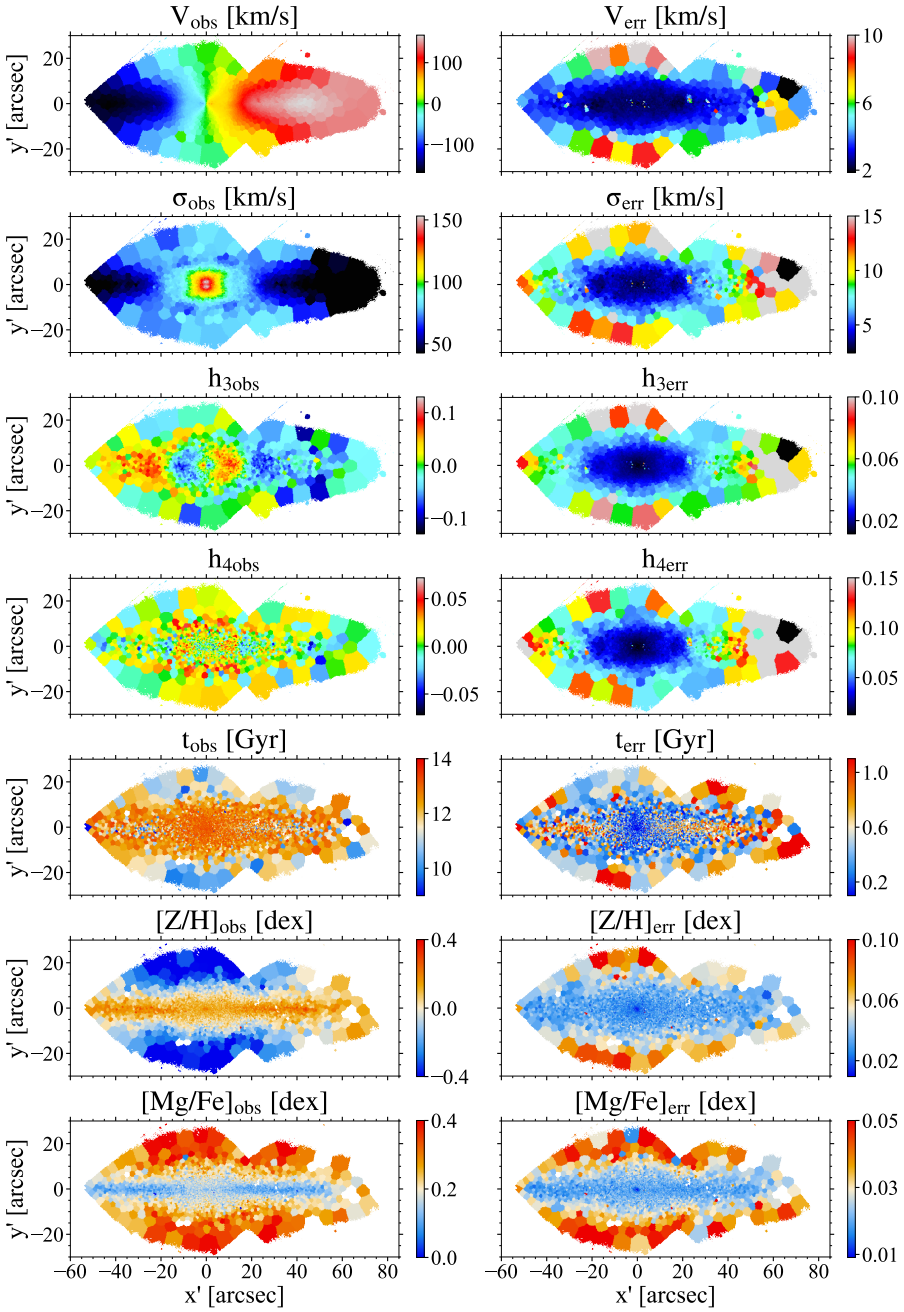


Fig. 2. Stellar kinematic and population maps (left panels) and their corresponding error maps (right panels) for NGC 1381. From top to bottom: Mean velocity, V; velocity dispersion, σ; third-order Gauss-Hermite coefficient, h_3; fourth-order Gauss-Hermite coefficient, h_4; stellar age, t; stellar metallicity, [Z/H]; and [Mg/Fe] abundance.

ism (Emsellem et al. 1994; Cappellari 2002), where each 2D Gaussian is assigned to either the triaxial bar component or the axisymmetric disc component. The MGE fitting results for NGC 1381, along with their corresponding contours, are presented in Table B.1 and Fig. B.1. These 2D Gaussians are then separately deprojected into 3D luminosity density using the viewing angles: the inclination θ (where $\theta = 90°$ corresponds to an edge-on view) and the bar azimuthal angle φ (where $\varphi = 0°$ corresponds to an end-on bar view and $\varphi = 90°$ to a side-on view). By multiplying the 3D luminosity density by a constant mass-to-light ratio, $M_\star/L$, and solving Poisson's equation, the potentials of both the stellar bar and the stellar disc are derived. We note that the bar and disc mentioned here are used to construct the stellar potential and are not necessarily the same as the dynamically decomposed bar and disc discussed later.

The dark matter potential follows a three-parameter generalised Navarro-Frenk-White profile (Navarro et al. 1996; Zhao 1996; see also Barnabè et al. 2012; Cappellari et al. 2013). The central black hole's contribution is modelled using a Plummer potential (van den Bosch et al. 2008) with a fixed softening length $r_s = 0.001$ arcsec, while the black hole mass $M_{\rm BH}$ is treated as a free parameter. Overall, the gravitational potential is determined by eight free parameters in the modelling: the inclination angle, θ; the bar azimuthal angle, φ; the stellar mass-to-light ratio, $M_\star/L$; the bar pattern speed, $\Omega_{\rm p}$; the dark matter concentration, c; the virial mass, M_{200}; the inner density slope of dark matter, γ; and the black hole mass, $M_{\rm BH}$. We note that adopting a constant $M_\star/L$ in the modelling does not influence our main results, although Martín-Navarro et al. (2021) reported the presence of an $M_\star/L$ gradient in this galaxy (see Appendix C).

In the given gravitational potential determined by a set of free parameters, initial conditions for $\sim 10^6$ orbits are sampled from the phase space and then integrated. After the integration,

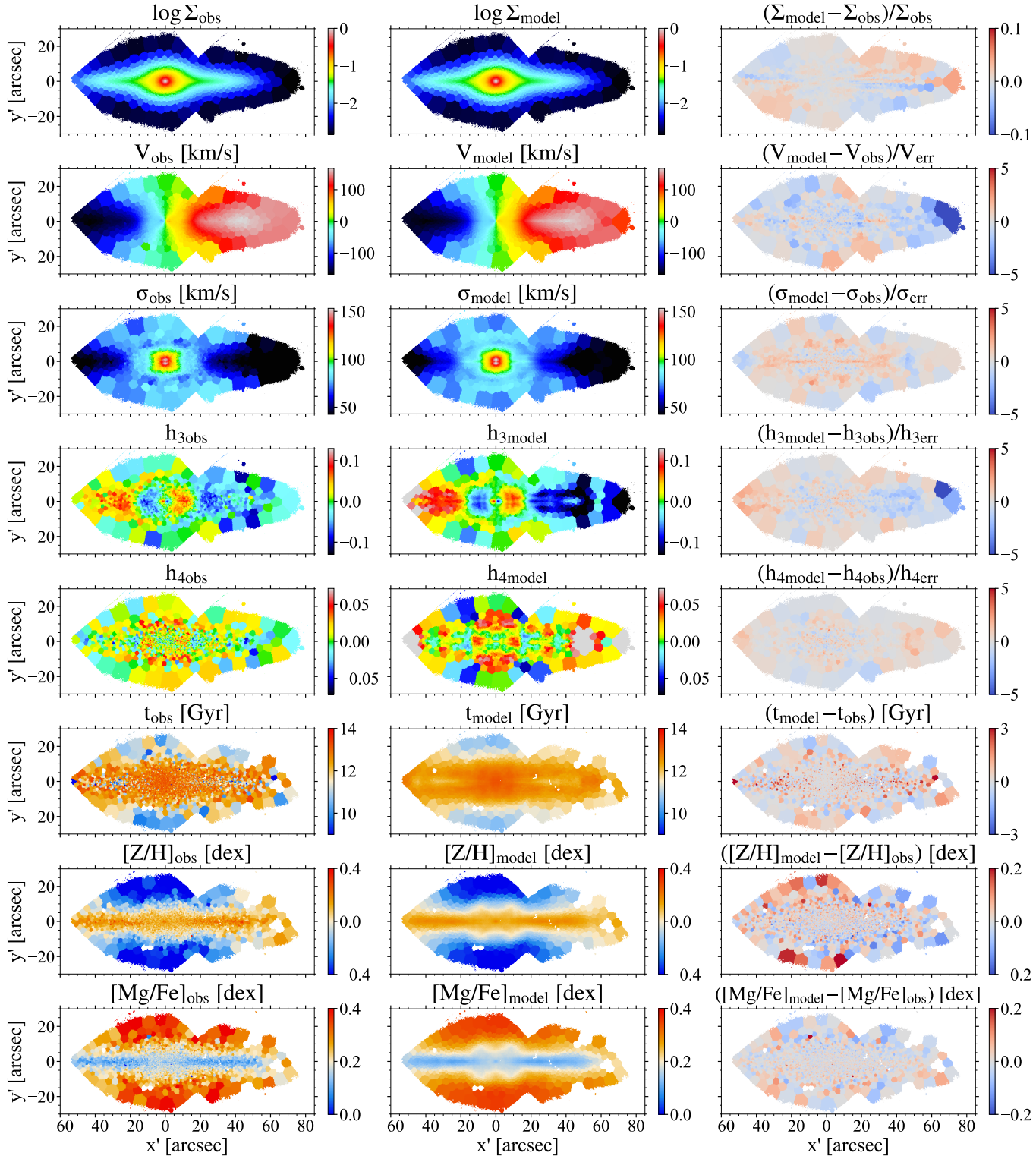


Fig. 3. Surface brightness, stellar kinematic data, stellar population data, and best-fitting model for NGC 1381. From left to right: Observations, model fittings, and residuals. From top to bottom: Logarithmic normalised surface brightness, log Σ; mean velocity, V; velocity dispersion, σ; third-order Gauss-Hermite coefficient, h_3; fourth-order Gauss-Hermite coefficient, h_4; stellar age, t; stellar metallicity, [Z/H]; and [Mg/Fe] abundance. The residual maps represent the relative deviations for surface brightness, the standardised residuals for stellar kinematics, and absolute differences for stellar populations.

the weights of these orbits are solved through the non-negative least squares method (Lawson & Hanson 1974), by matching the MGE-fitted 2D surface brightness, the MGE-deprojected 3D luminosity density, and the observed kinematic data. The goodness of the model (χ^2) is evaluated by computing the sum of squared residuals between model-fitted and observed kinematic maps, including the velocity (V), velocity dispersion (σ), third-order and fourth-order Gauss-Hermite coefficients (h_3 and h_4),

which is written as

$$\chi^2 = \sum_{i=1}^{N_{\rm obs}} \left[\left(\frac{V^i_{\rm obs} - V^i_{\rm model}}{V^i_{\rm err}} \right)^2 + \left(\frac{\sigma^i_{\rm obs} - \sigma^i_{\rm model}}{\sigma^i_{\rm err}} \right)^2 + \left(\frac{h^i_{3\rm obs} - h^i_{3\rm model}}{h^i_{3\rm err}} \right)^2 + \left(\frac{h^i_{4\rm obs} - h^i_{4\rm model}}{h^i_{4\rm err}} \right)^2 \right]. \quad (1)$$

The best-fitting model with the minimum χ^2 is found by iteratively searching the free parameter space $(\theta, \varphi, M_\star/L, \Omega_{\rm p}, c, M_{200}, \gamma, M_{\rm BH})$. Starting with initial guesses, models with lower χ^2 are selected and new models are generated by exploring nearby regions in the parameter space. This process repeats until the minimum χ^2 ($\chi^2_{\rm min}$) is reached, ensuring all surrounding models are calculated. The model with $\chi^2_{\rm min}$ is identified as the best-fitting model, which is taken as the default model in our analysis.

We present the surface brightness and stellar kinematic maps of the best-fitting model for NGC 1381 in Fig. 3. The features of the stellar kinematics are well recovered, including the anti-correlated, correlated, and anti-correlated again h_3–V relation along the galaxy's major axis, which correspond to the signatures of the nuclear disc, bar, and main disc, respectively. The parameter space we explored and the model-predicted enclosed mass profiles are displayed in Figs. C.1 and C.2, respectively.

3.2. Decomposing galaxies based on stellar orbits

Based on the kinematic and morphological properties of stellar orbits, we decomposed the galaxy into six components: a nuclear disc, a bar, a bulge, a thin disc, a thick disc, and a stellar halo. These properties include: (1) orbital circularity, λ_z; (2) time-averaged orbital radius, R; (3) axis ratio, $p_{\rm orb}$ in the x-y plane (bar's rotating frame); (4) axis ratio, $q_{\rm orb,0}$ in the x_0-z plane (inertial frame); and (5) vertical height, $z_{\rm orb}$.

The circularity, λ_z, quantifying the orbit's angular momentum L_z in the inertial frame (x_0, y_0, z), is defined as

$$\lambda_z = \overline{L_z}/(R \times \overline{V_{\rm rms}}), \quad (2)$$

where $\overline{L_z} = \overline{x_0 v_{y0} - y_0 v_{x0}}$, $R = \overline{\sqrt{x_0^2 + y_0^2 + z^2}}$, and $\overline{V_{\rm rms}} = \overline{\sqrt{v_{x0}^2 + v_{y0}^2 + v_z^2 + 2v_{x0}v_{y0} + 2v_{x0}v_z + 2v_{y0}v_z}}$. Dynamically cold orbits with $\lambda_z \sim 1$ (rotation-dominated) mainly contribute to the disc components, while dynamically hot orbits with $\lambda_z \sim 0$ (dispersion-dominated) or $\lambda_z < 0$ (retrograde) usually belong to the bulge or stellar halo. A discussion of the influence of the cross terms in $\overline{V_{\rm rms}}$ is provided in Appendix D.

In a typical barred galaxy, the circularity increases with radius in the bar-dominated inner region, whereas it remains dynamically cold at all radii in the disc-dominated outer regions (see the left panel of Fig. 5). Therefore, the dynamical bar length, $R_{\rm bar}$, is defined as the radius where dynamically cold orbits ($\lambda_z \geq 0.8$) begin to dominate. For NGC 1381, we calculated the cold orbit fraction, $f_{\rm cold}$, within a 0.5 kpc moving average and identified $R_{\rm bar}$ as the smallest radius at which $f_{\rm cold} \geq 0.5$. In our models, we treat $R_{\rm bar}$ as a boundary to distinguish the galaxy's inner regions (nuclear disc, bar, and bulge) from the outer regions (thin disc, thick disc, and stellar halo), where $R_{\rm bar}$ equals 23.6 arcsec (2.24 kpc) for the best-fitting model. The bar length ($R_{\rm bar}$) provides a natural separation of the bar and the nuclear disc embedded within it from the outer thin disc, whereas the radial division between the bulge, thick disc, and halo remains somewhat uncertain. For simplicity, in this work we adopt $R_{\rm bar}$ as a divider for the bulge, thick disc, and halo, and the halo here can be understood as the less bound part of the bulge. We note that the time-averaged radius of the orbits (R) scales with the orbital binding energy ($E_{\rm bind}$). The rationale for using this boundary is further discussed in Appendix E.

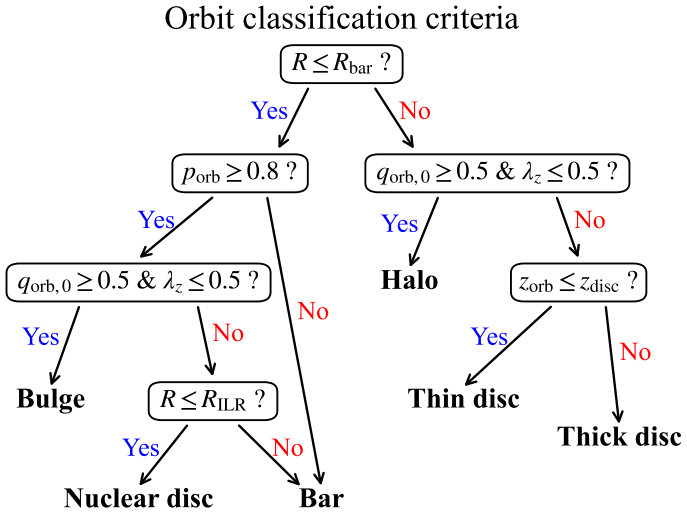


Fig. 4. Orbit classification criteria used in our dynamical decomposition. Each box represents a criterion. Five properties are adopted to classify the orbits: (1) circularity, λ_z; (2) time-averaged radius, R; (3) axis ratio, $p_{\rm orb}$, in the x-y plane (the bar's rotating frame); (4) axis ratio, $q_{\rm orb,0}$, in the x_0-z plane (the inertial frame); and (5) vertical height, $z_{\rm orb}$. The dynamical bar length, $R_{\rm bar}$, and the radius of the inner Lindblad resonance, $R_{\rm ILR}$, are determined from our model results, while the separation threshold of vertical height, $z_{\rm disc} = 7$ arcsec, is estimated from Fig. 4 of Pinna et al. (2019a). Six components were derived from the decomposition: a nuclear disc, a bar, a bulge, a thin disc, a thick disc, and a stellar halo.

The radius of the inner Lindblad resonance, $R_{\rm ILR}$, is defined as the radius at which a star's epicyclic frequency (κ) and azimuthal frequency ($\Omega(R)$) satisfy $\Omega(R) - \kappa/2 = \Omega_{\rm p}$. This resonance radius can be calculated directly from the gravitational potential and is consistently smaller than the bar length ($R_{\rm ILR} < R_{\rm bar}$). The orbits inside $R_{\rm ILR}$, which can be dynamically cold and/or perpendicular to the bar (e.g. Contopoulos & Mertzanides 1977; Athanassoula 1992a,b; Binney & Tremaine 2008), make up the nuclear disc in our modelling. For the best-fitting model, we derived $R_{\rm ILR} = 16.6$ arcsec (1.57 kpc).

Based on the time-averaged amplitudes of orbital trajectories, three orbital quantities are calculated: (1) the axis ratio, $p_{\rm orb}$, in the bar's rotating frame; (2) the axis ratio, $q_{\rm orb,0}$, in the inertial frame; and (3) the vertical height, $z_{\rm orb}$. These quantities are expressed as

$$p_{\rm orb} = \frac{\overline{|y - \overline{y}|}}{\overline{|x - \overline{x}|}}, \quad q_{\rm orb,0} = \frac{\overline{|z - \overline{z}|}}{\overline{|x_0 - \overline{x_0}|}}, \quad z_{\rm orb} = \overline{|z|}. \quad (3)$$

The axis ratio, $p_{\rm orb}$, is adopted to distinguish bar orbits, which are elongated with the bar, from nuclear disc and bulge orbits. The axis ratio, $q_{\rm orb,0}$, together with λ_z, is used to separate the disc components from the bulge and stellar halo. The vertical height, $z_{\rm orb}$, distinguishes between the thin and thick discs, using a separation threshold of $z_{\rm disc} = 7$ arcsec (0.66 kpc) estimated from Pinna et al. (2019a).

Combining these properties, we present the detailed orbit classification criteria in Fig. 4, and thus the dynamical

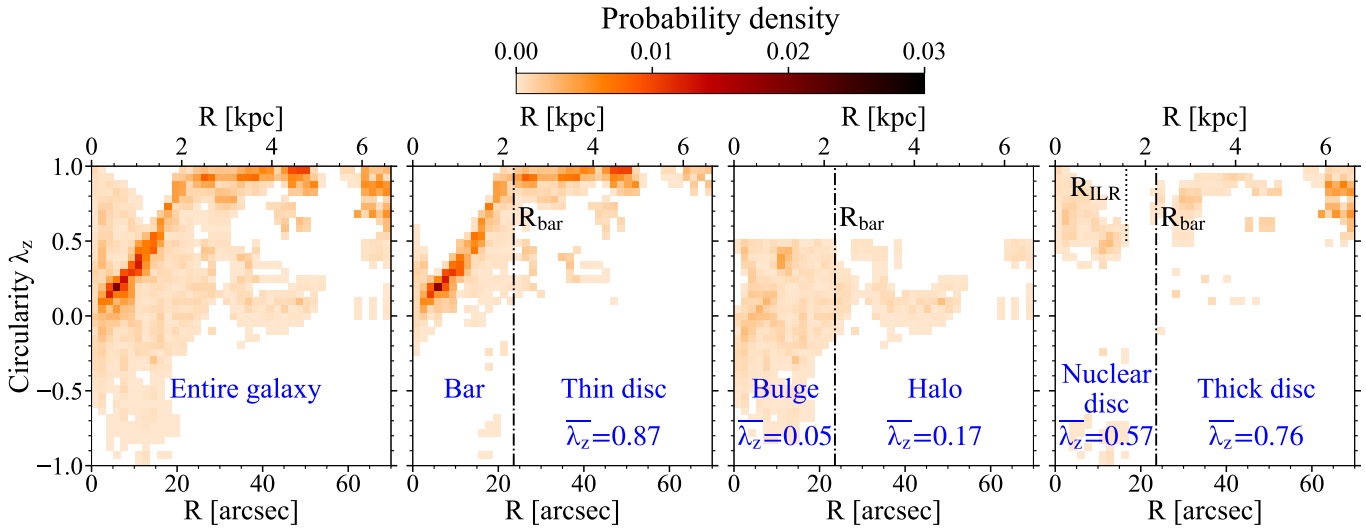


Fig. 5. Probability density distributions of stellar orbits in the λ_z–R phase space for the best-fitting model of NGC 1381. The leftmost panel shows the stellar orbit distribution for the entire galaxy. The three remaining panels each display two dynamical components, separated by a vertical dashed line indicating the bar length ($R_{\rm bar}$ = 2.24 kpc): (1) the bar and thin disc; (2) the bulge and halo; and (3) the nuclear disc and thick disc. The dotted line in the rightmost panel represents the radius of the inner Lindblad resonance ($R_{\rm ILR}$ = 1.57 kpc). The probability densities of all orbits within $R \leq 70$ arcsec (6.64 kpc) are normalised to unity, with their values indicated by the colour bar. The mean circularities ($\overline{\lambda_z}$) of the thin disc, bulge, halo, nuclear disc, and thick disc are indicated.

decomposition of the galaxy can be achieved. Fig. 5 displays the decomposed stellar orbit distributions in the λ_z–R phase space for the best-fitting model of NGC 1381 (see Appendix F for a comparison with the stellar orbit distributions of the unbarred model from Ding et al. 2023). Other models within the 1σ confidence level were decomposed using the same criteria (see Sect. 3.4 for the definition of uncertainties). This galaxy is divided into six components: a rigidly rotating bar (λ_z strongly correlated with R); a dynamically hot bulge and halo ($\overline{\lambda_z}$ = $0.05^{+0.03}_{-0.07}$ and $0.17^{+0.13}_{-0.08}$, respectively); a dynamically cold thin disc ($\overline{\lambda_z}$ = $0.87^{+0.02}_{-0.03}$); a thick disc with slightly slower rotation than the thin disc ($\overline{\lambda_z}$ = $0.76^{+0.04}_{-0.03}$); and a dynamically warm nuclear disc ($\overline{\lambda_z}$ = $0.57^{+0.12}_{-0.11}$). The spatial distributions of luminosity-weighted mean velocity and velocity dispersion for each component are shown in Fig. G.1.

3.3. Tagging the stellar orbits with stellar populations

Following Jin et al. (2025b), we separated the orbits belonging and not belonging to the bar into two distinct λ_z–R phase spaces. We then used the Voronoi 2D binning method to divide orbits in each λ_z–R phase space into different orbit bundles, assuming that each orbit bundle k has a simple stellar population with age (t_k), metallicity ([Z/H]$_k$), and [Mg/Fe] abundance ([Mg/Fe]$_k$) to be determined.

By projecting the orbits onto the observation plane, the model-recovered, luminosity-weighted stellar population in the i-th aperture can be expressed as

$$p^i_{\rm model} = \frac{\sum_{k=1}^{N_b} p_k f^i_k}{\sum_{k=1}^{N_b} f^i_k}, \tag{4}$$

where the quantity p represents age, metallicity, or [Mg/Fe] abundance. Here, N_b denotes the total number of orbit bundles, while f^i_k represents the luminosity contribution from the k-th orbit bundle within the i-th aperture.

Similar to the kinematics, the chi-square difference between model-fitted maps and observed data is given by

$$\chi^2_p = \sum_{i=1}^{N_{\rm obs}} \left(\frac{p^i_{\rm obs} - p^i_{\rm model}}{p^i_{\rm err}} \right)^2. \tag{5}$$

We solved the stellar population parameter of each orbit bundle, p_k, by minimising χ^2_p for age, metallicity, and [Mg/Fe] abundance independently via the bounded-variable least squares method (implemented in Python's SciPy[2]), with the boundaries of stellar population parameters set as

$$\begin{cases} \min(t^i_{\rm obs}) \leq t_k \leq \min[\max(t^i_{\rm obs}) + \Delta(t^i_{\rm obs}), 14\,{\rm Gyr}], \\ \min([{\rm Z/H}]^i_{\rm obs}) \leq [{\rm Z/H}]_k \leq \max([{\rm Z/H}]^i_{\rm obs}) + \Delta([{\rm Z/H}]^i_{\rm obs}), \\ \min([{\rm Mg/Fe}]^i_{\rm obs}) - \Delta([{\rm Mg/Fe}]^i_{\rm obs}) \leq [{\rm Mg/Fe}]_k \leq \max([{\rm Mg/Fe}]^i_{\rm obs}), \end{cases} \tag{6}$$

where Δ represents the standard deviation of the observed data. This Δ term is added because the galaxy's central region is a mixture of multiple stellar populations, allowing for the possible presence of intrinsically older, more metal-rich, and α-poor stellar populations than the observed data. In contrast, no such Δ is needed for the younger, more metal-poor, and α-rich stellar populations in the galaxy's outer regions, which are dominated by the thick disc. Moreover, the stellar populations there have larger uncertainties compared to the inner regions, so setting the minimum or maximum values of the observed maps already provides sufficient tolerance. The recovered stellar population maps of the best-fitting model are shown in Figs. 3 (version A), A.1 (version B), and A.2 (version C).

3.4. Model uncertainties

In our models, we estimated the uncertainties by perturbing the observed data maps. For purely kinematic properties, the uncertainties originate from the stellar kinematic maps; for properties

[2] https://scipy.org/

related to stellar populations, the uncertainties are estimated by considering the contributions from both stellar kinematics and stellar populations.

The kinematic confidence level of the modelling is used to estimate the uncertainties of the free parameters $(\theta, \varphi, M_\star/L, \Omega_p, c, M_{200}, \gamma, M_{BH})$, as well as of the properties presented in Sects. 3.2, 4.1, and 4.2. This confidence level was calculated by perturbing the kinematic maps $(V^i_{obs}, \sigma^i_{obs}, h^i_{3\,obs}, h^i_{4\,obs})$ 1000 times, adding Gaussian noise based on their error maps $(V^i_{err}, \sigma^i_{err}, h^i_{3\,err}, h^i_{4\,err})$ estimated from the pPXF fitting. The perturbed kinematic maps were then point-symmetrised in the same way as the original maps. Fixing the best-fitting gravitational potential, we recomputed the orbit weights for each perturbed kinematic map and obtained 1000 new χ^2 values, whose distribution is approximately Gaussian. The kinematic confidence levels were defined based on this distribution: the 1σ, 2σ, and 3σ confidence levels correspond to χ^2 variations within the $\pm1\sigma$ (68%), $\pm2\sigma$ (95%), and $\pm3\sigma$ (>99%) regions of this distribution, respectively. We took the 1σ confidence level ($\chi^2 - \chi^2_{min} \leq \Delta\chi^2_{CL}$) as the uncertainties. Approximately 1400 models (1400 combinations of free parameters) were located within the 1σ confidence level and were adopted to estimate the uncertainties.

The 1σ uncertainties of the model-predicted stellar ages incorporate contributions from two sources: the observed stellar kinematic maps and the observed stellar age maps. To quantify the uncertainties arising from kinematics (Δt_{kin}), we first fixed the observed stellar age maps and calculated the stellar ages of each component for all models within the kinematic 1σ confidence level. We then took the standard deviation of these ages across different models as Δt_{kin}. To estimate the uncertainties from the stellar age maps (Δt_{age}), we fixed the orbit libraries and weights of the best-fitting model. We then perturbed the observed stellar age maps 1000 times according to their error maps (in the same way as we perturbed the kinematic maps) and recalculated the stellar ages for each component. The standard deviations of the resulting age distributions were taken as Δt_{age}. Assuming that the uncertainties from kinematics and age maps are independent, the total 1σ uncertainties for stellar ages (Δt_{all}) were derived using error propagation: $\Delta t^2_{all} = \Delta t^2_{kin} + \Delta t^2_{age}$. The uncertainties of stellar metallicities ([Z/H]) and [Mg/Fe] abundances were estimated similarly. These uncertainties are used in Sect. 4.3 (Figs. 12 and 13).

4. Dynamical structures and their chemical properties

In this section, we analyse the properties of NGC 1381's dynamical components derived from our barred population-orbit superposition models, including the bar pattern speed, bar length, and corotation radius (Sect. 4.1); the 3D luminosity distributions of the different structures (Sect. 4.2); and the stellar populations of each component (Sect. 4.3).

4.1. Bar pattern speed, bar length, and corotation radius

From the gravitational potential Φ derived from the modelling, the angular velocity profile $\Omega(R)$ of the galaxy on the disc plane ($z = 0$) is

$$\Omega(R) = \frac{v_{circ}(R)}{R} = \sqrt{\frac{1}{R}\frac{\partial\Phi}{\partial R}\Big|_{z=0}}. \quad (7)$$

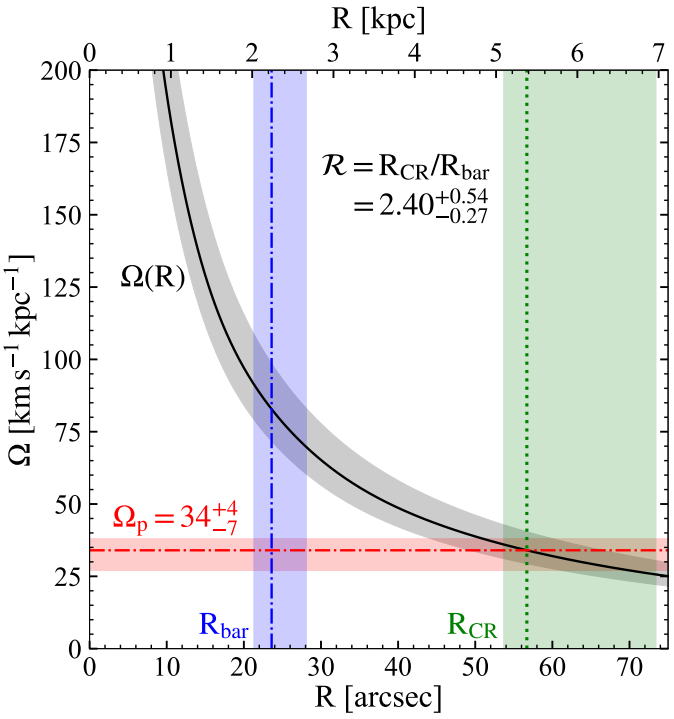


Fig. 6. Analysis of corotation resonance for NGC 1381. The black solid line, red dashed line, blue dashed line, and green dotted line represent the angular velocity profile ($\Omega(R)$), bar pattern speed (Ω_p), bar length (R_{bar}), and corotation radius (R_{CR}) of the best-fitting model, respectively. The corresponding shaded regions indicate uncertainties calculated from models within the 1σ confidence level. The dimensionless bar rotation rate, $\mathcal{R} = R_{CR}/R_{bar}$, is labelled.

For each model within the 1σ confidence level, the bar pattern speed (Ω_p), being a free parameter of the potential, was already determined. We further calculated the dynamical bar length (R_{bar}; see Sect. 3.2) and $\Omega(R)$. The corotation radius, R_{CR}, defined as the radius where the angular velocity matches the bar pattern speed ($\Omega(R) = \Omega_p$), was then derived accordingly. Finally, we computed the dimensionless bar rotation rate, $\mathcal{R} = R_{CR}/R_{bar}$, which is adopted to distinguish fast bars ($1.0 \leq \mathcal{R} \leq 1.4$), slow bars ($\mathcal{R} > 1.4$), and ultrafast bars ($\mathcal{R} < 1.0$; Debattista & Sellwood 2000; Buta & Zhang 2009; Aguerri et al. 2015). All these quantities are illustrated in Fig. 6. We derived $\Omega_p = 34^{+4}_{-7}$ km s^{-1} kpc^{-1}, $R_{bar} = 23.6^{+4.5}_{-2.3}$ arcsec ($2.24^{+0.43}_{-0.22}$ kpc), and $R_{CR} = 56.7^{+16.7}_{-3.0}$ arcsec ($5.38^{+1.59}_{-0.28}$ kpc). These yield a slow bar with $\mathcal{R} = 2.40^{+0.54}_{-0.27}$.

4.2. Luminosity distribution of dynamical components

Using the orbital weights and trajectories from the best-fitting model, we reconstructed the 3D luminosity distributions for the six dynamical components. Fig. 7 displays these distributions projected onto the x-y, x-z, and y-z planes. The 3D morphologies of different components are well distinguished: the nuclear disc occupies the galaxy's inner regions ($\lesssim$20 arcsec); the bar is BP/X-shaped; the thin disc dominates the galaxy's outer regions ($\gtrsim$25 arcsec); the bulge is spheroidal; the thick disc is vertically extended; and the stellar halo is radially diffuse. We note that the 'holes' in the thin and thick disc components arise from our dynamical classification criteria: orbits with $R \leq R_{bar}$ (i) follow the bar's rigid rotation, (ii) belong to the dispersion-dominated bulge, or (iii) are rotation-dominated orbits within

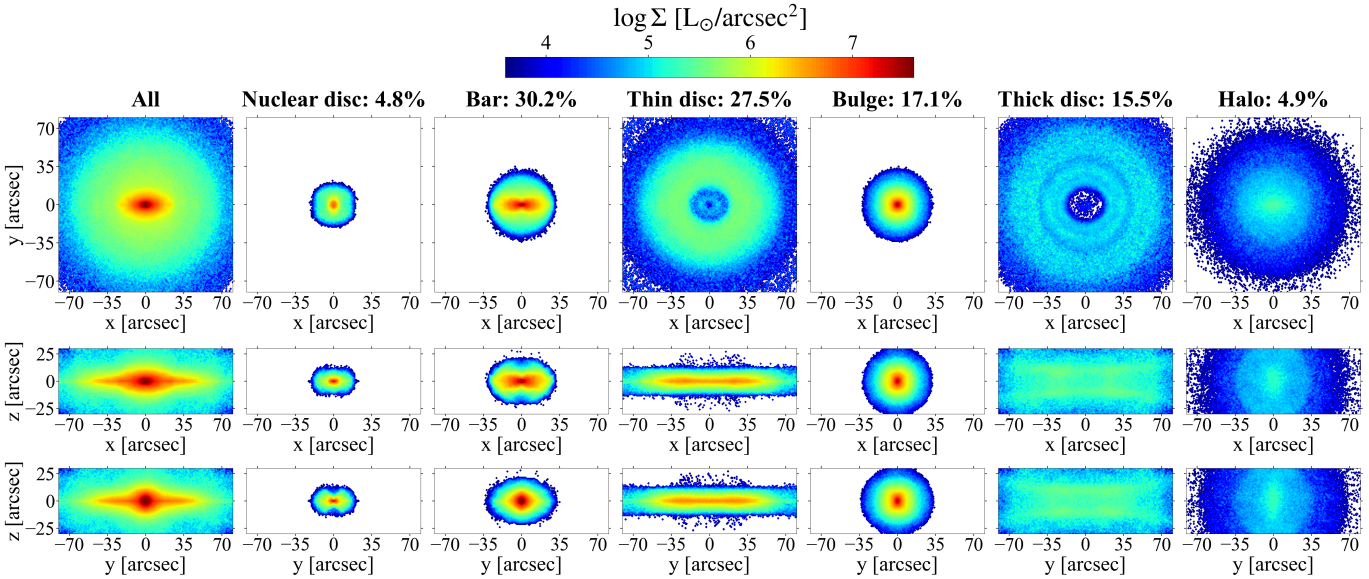


Fig. 7. Luminosity distributions of dynamical components in the best-fitting model of NGC 1381. From top to bottom: Logarithmic surface brightness on the x-y (face-on), x-z (edge-on and bar side-on), and y-z (edge-on and bar end-on) planes, respectively. From left to right: Entire galaxy, nuclear disc, bar, thin disc, bulge, thick disc, and stellar halo. The luminosity fraction of each component is labelled.

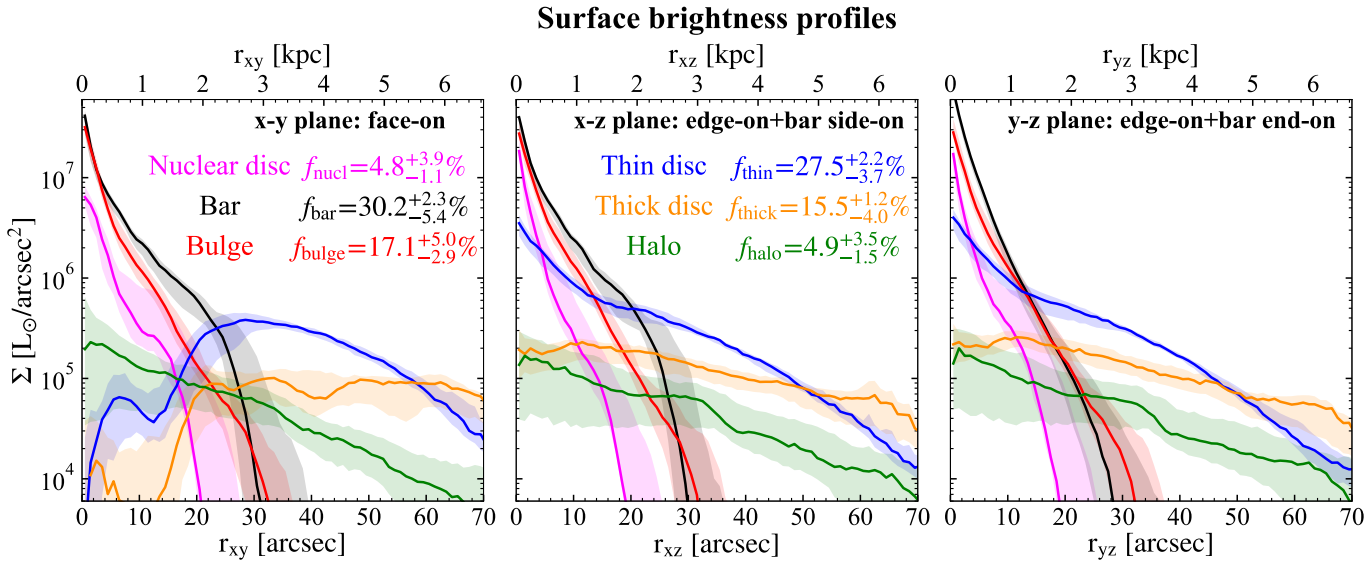


Fig. 8. Surface brightness profiles for the dynamical components in the models of NGC 1381. From left to right: Surface brightness profiles on the x-y ($r_{xy} = \sqrt{x^2+y^2}$), x-z ($r_{xz} = \sqrt{x^2+z^2}$), and y-z ($r_{yz} = \sqrt{y^2+z^2}$) planes. The solid curves represent the best-fitting profiles of different components: nuclear disc (magenta), bar (black), bulge (red), thin disc (blue), thick disc (orange), and stellar halo (green). The corresponding shaded regions indicate uncertainties calculated from models within the 1σ confidence level. The luminosity fraction of each component, together with its uncertainty, is shown.

the inner Lindblad resonance that belong to the nuclear disc (see Fig. 5). Such 'holes' also emerged in our previous simulation tests, where our model results match the truth well (Jin et al. 2025b). The substructures, including the BP/X-shaped structure in the nuclear disc and the ring-like structure in the thick disc, are artefacts of model fluctuations, and they change within the 1σ confidence level across different models.

Similarly, we derived the luminosity distributions of each component for each model within the 1σ confidence level and plotted their surface brightness profiles on the x-y, x-z, and y-z planes in Fig. 8. The profiles of the galaxy's inner components (nuclear disc, bar, and bulge) exhibit similarly steep radial declines. In contrast, the thin and thick discs display more complex trends: The inner regions of both discs ($r \lesssim 20$ arcsec; 2 kpc) exhibit 'holes' in the x-y plane, while they display approximately constant gradients in the x-z and y-z planes, with the thin disc being less vertically extended compared to the thick disc. The stellar halo profiles are approximately exponential across all projections. These complex surface brightness profiles derived from our dynamical models indicate that the underlying structures (with different physical origins) might deviate significantly from the assumptions adopted in traditional photometric decomposition methods.

We calculated the luminosity fractions of all components in the entire galaxy, which are displayed in Fig. 8: the nuclear disc with $f_{\rm nucl} = 4.8^{+3.9}_{-1.1}\%$; the bar with $f_{\rm bar} = 30.2^{+2.3}_{-5.4}\%$; the bulge

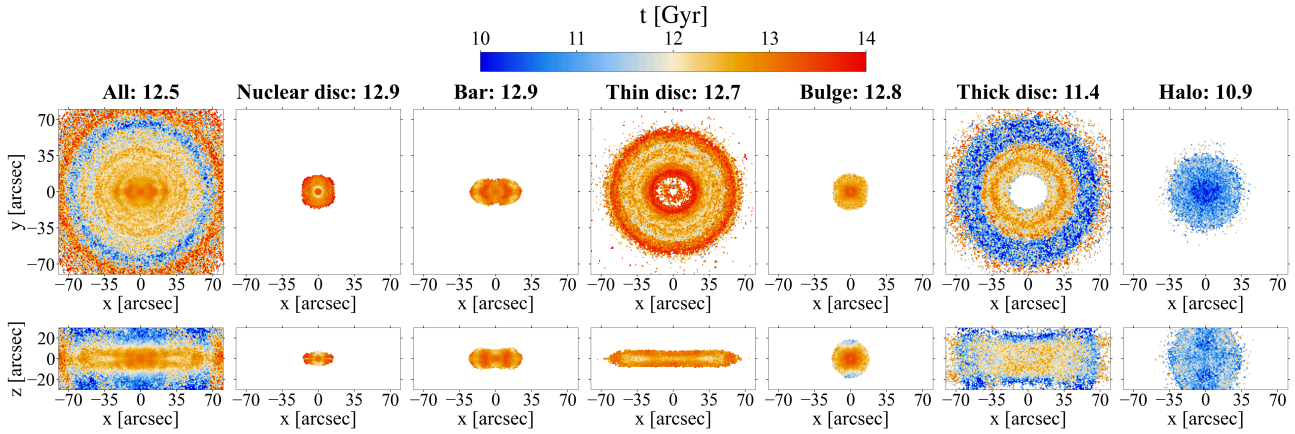


Fig. 9. Spatial distributions of luminosity-weighted stellar ages for dynamical components in the best-fitting model of NGC 1381, projected onto the x-y (top) and x-z (bottom) planes. From left to right: Entire galaxy, nuclear disc, bar, thin disc, bulge, thick disc, and stellar halo. For each component, only pixels above specified brightness thresholds are plotted. The mean stellar ages of the entire galaxy and its components are labelled.

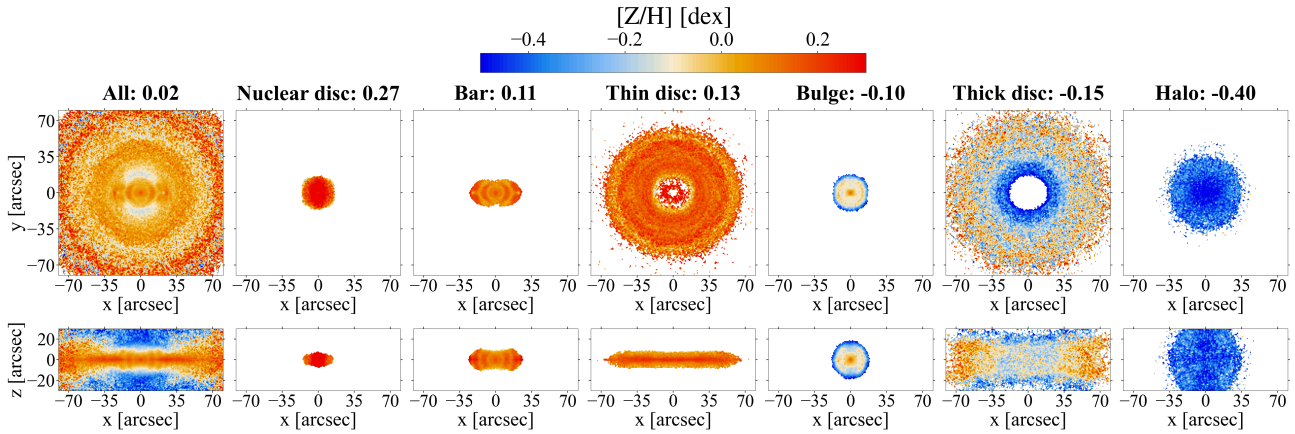


Fig. 10. Same as Fig. 9 but for luminosity-weighted stellar metallicities ([Z/H]).

with $f_{\rm bulge} = 17.1^{+5.0}_{-2.9}\%$; the thin disc with $f_{\rm thin} = 27.5^{+2.2}_{-3.7}\%$; the thick disc with $f_{\rm thick} = 15.5^{+1.2}_{-4.0}\%$; and the stellar halo with $f_{\rm halo} = 4.9^{+3.5}_{-1.5}\%$. These results demonstrate that the galaxy is dominated by the bar and thin disc, with some contributions from the thick disc and bulge, while the nuclear disc and halo account for minor fractions.

4.3. Stellar populations of dynamical components

As mentioned in Sect. 3.3, we derived the stellar age for each orbit in our models. We therefore calculated the 3D luminosity-weighted stellar age distributions for each decomposed component in the best-fitting model. Fig. 9 presents these distributions through their projections onto the x-y and x-z planes. We also show the mean stellar age for each component in the figure. All components are old, with the nuclear disc, bar, thin disc, and bulge sharing similar ages, while the thick disc and stellar halo are slightly younger.

Following our analysis of stellar ages, we similarly derived the luminosity-weighted stellar metallicity ([Z/H]) and [Mg/Fe] abundance distributions in the best-fitting model and presented them in Figs. 10 and 11, respectively. The corresponding metallicity and [Mg/Fe] abundance profiles are shown in Fig. H.1. Based on the mean [Z/H] and [Mg/Fe] values, the six dynamical components can be separated into two groups with distinct stellar populations: (1) the metal-rich ([Z/H] > 0) and α-poor ([Mg/Fe] < 0.2) nuclear disc, bar, and thin disc; and (2) the metal-poor ([Z/H] < 0) and α-rich ([Mg/Fe] > 0.2) bulge, thick disc, and stellar halo. These results indicate distinct physical origins for the two groups.

For each model within the 1σ confidence level, we calculated the luminosity-weighted mean stellar ages, metallicities, and [Mg/Fe] abundances of all dynamical components and presented them in Fig. 12. For each data version (A, B, and C), obvious differences are revealed in the mean metallicities and [Mg/Fe] abundances: The bulge, thick disc, and stellar halo are consistently metal-poor and α-rich compared to the nuclear disc, bar, and thin disc within the 1σ confidence level. Although version C has systematic offsets in stellar metallicity and [Mg/Fe] abundance compared to versions A and B, the relative differences in stellar populations between different components are consistent across all versions. This indicates that our main findings are not affected. All dynamical components are generally old (8–14 Gyr), with the thick disc and stellar halo being slightly younger than the nuclear disc, bar, and thin disc. The bulge is either younger than (version C) or comparable in age to (versions A and B) the nuclear disc, bar, and thin disc.

To better investigate the origins of different structures, we further computed their stellar metallicity gradients (∇[Z/H]) and

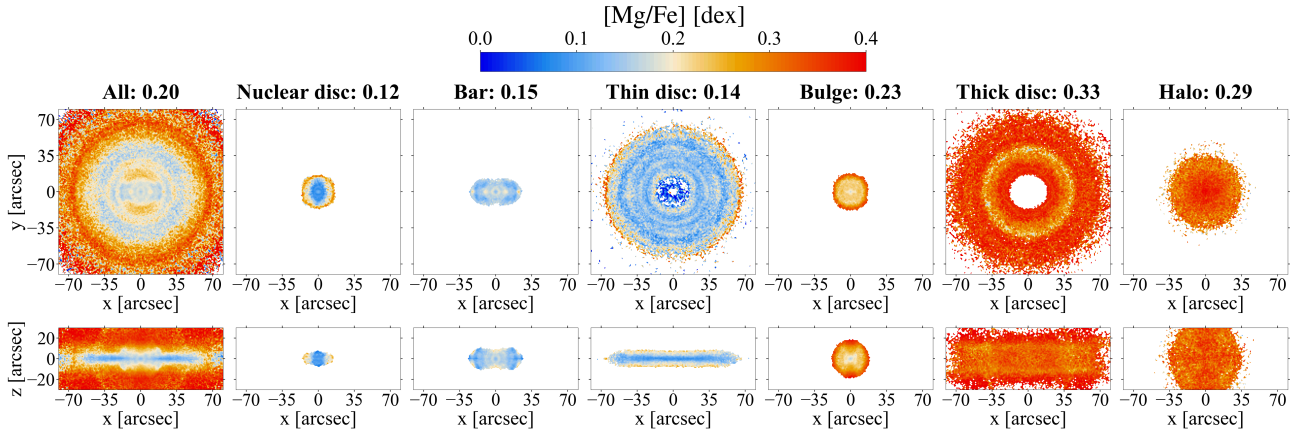


Fig. 11. Same as Fig. 9 but for luminosity-weighted [Mg/Fe] abundances.

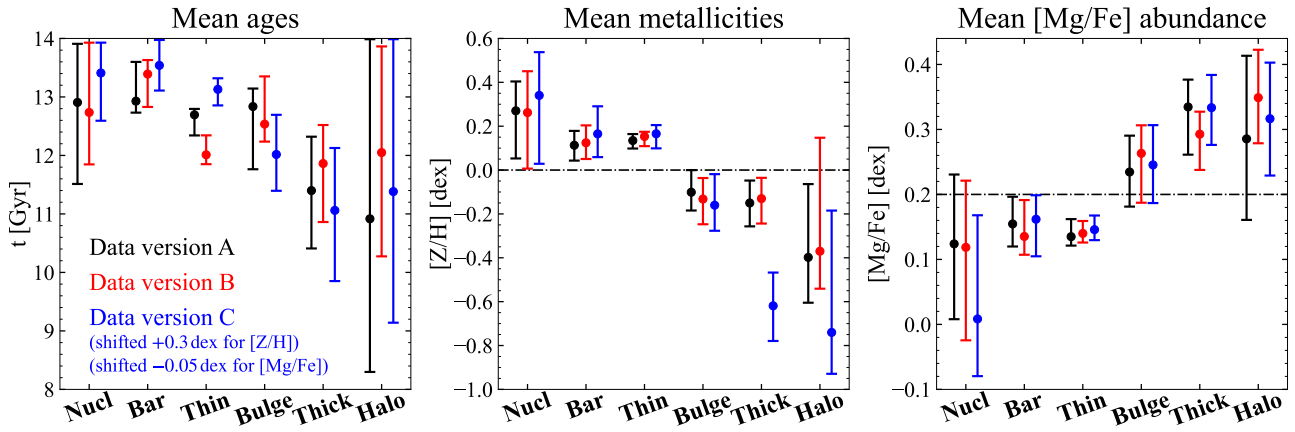


Fig. 12. Luminosity-weighted mean stellar ages (left), stellar metallicities (middle), and [Mg/Fe] abundances (right) of different components derived from the three data versions: A (black), B (red), and C (blue). To facilitate a direct comparison, the results for version C have been shifted by 0.3 dex in metallicity and −0.05 dex in [Mg/Fe] abundance to account for systematic offsets relative to versions A and B. In each panel, the x-axis labels (from left to right) represent the nuclear disc, bar, bulge, thin disc, thick disc, and stellar halo. The dots represent the values of the best-fitting model, and the error bars indicate the 1σ confidence level. The horizontal dashed lines in the middle and right panels represent the reference values ([Z/H] = 0.0 and [Mg/Fe] = 0.2 for versions A and B; and [Z/H] = −0.3 and [Mg/Fe] = 0.25 for version C).

[Mg/Fe] abundance gradients (∇[Mg/Fe]). These gradients were determined by applying a luminosity-weighted linear regression to the radial profiles, and are shown in Fig. 13. We note that the age gradients are not shown due to their large uncertainties. For metallicity gradients, only the bulge exhibits a significant negative gradient ($\nabla[Z/H]_{\rm bulge} < 0$ for all data versions), while all other components show no significant trends (uncertainties encompass zero). For [Mg/Fe] abundance gradients, none of the components display any significant positive or negative gradients.

5. Discussion

5.1. An ancient slow bar with $\mathcal{R} > 2$

We derived a bar rotation rate of $\mathcal{R} = 2.40^{+0.54}_{-0.27}$ for NGC 1381, corresponding to a slow bar. This rate depends directly on the bar length, $R_{\rm bar}$, the bar pattern speed, $\Omega_{\rm p}$, and the angular velocity profile, $\Omega(R)$. In this subsection, we discuss the possible reasons for such a slow bar in NGC 1381.

Statistical studies have reported that most bars in nearby galaxies are fast bars ($1.0 \leq \mathcal{R} \leq 1.4$), with average bar pattern speeds of approximately 20−50 km s^{-1} kpc^{-1}, average bar lengths of roughly 3−6 kpc, and average corotation radii of around 4−10 kpc (e.g. Rautiainen et al. 2008; Aguerri et al. 2015; Guo et al. 2019; Cuomo et al. 2020; Garma-Oehmichen et al. 2022; Ruiz-García et al. 2024). The discrepancies in mean values among these studies arise from differences in sample selection and methodology, with both bar lengths and corotation radii strongly correlated with stellar masses. However, because measuring bar pattern speeds requires high-quality data, most galaxies in these samples ($M_\star \gtrsim 3 \times 10^{10}\,{\rm M}_\odot$) are more massive than NGC 1381 ($M_\star = 1.65^{+0.13}_{-0.38} \times 10^{10}\,{\rm M}_\odot$ from our models and $2.25 \times 10^{10}\,{\rm M}_\odot$ reported by Iodice et al. 2019a). Compared to these statistical averages, our modelling indicates that NGC 1381, with a smaller stellar mass, hosts a relatively short bar ($R_{\rm bar} = 2.24^{+0.43}_{-0.22}$ kpc), but its pattern speed ($\Omega_{\rm p} = 34^{+4}_{-7}$ km s^{-1} kpc^{-1}) and corotation radius ($R_{\rm CR} = 5.38^{+1.59}_{-0.28}$ kpc) are comparable to the typical values.

According to the current paradigm of bar dynamics, the formation of nuclear discs is driven by gas inflow that is channelled by bars (e.g. Athanassoula 2003; Kormendy & Kennicutt 2004; Gadotti 2011). Therefore, the stellar age of the nuclear disc, $t_{\rm nucl}$, is a good tracer of the bar formation time, $t_{\rm bar,form}$ (e.g. de Sá-Freitas et al. 2023, 2025). The nuclear disc of NGC 1381 is very old ($t_{\rm nucl} \sim 13$ Gyr), indicating its formation in the early Universe. After the galaxy entered the cluster approximately 8–12 Gyr ago (e.g. Iodice et al. 2019b; Ding et al.

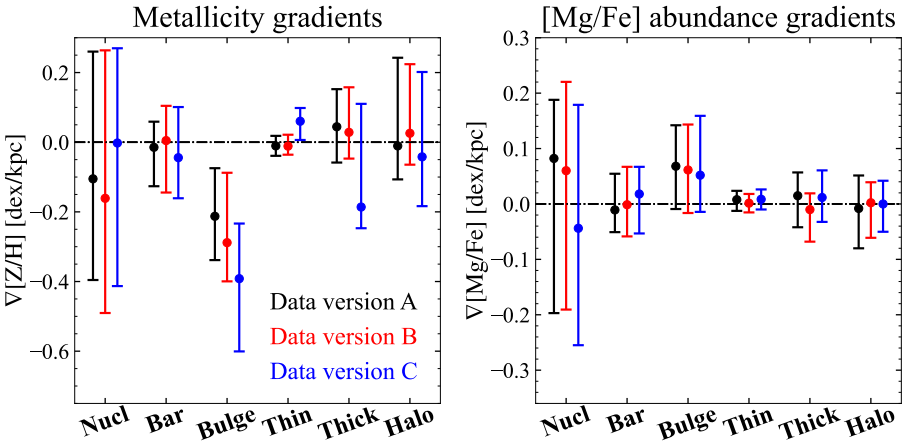


Fig. 13. Stellar metallicity gradients (left) and [Mg/Fe] abundance gradients (right) of different components derived from the three data versions: A (black), B (red), and C (blue). The x-axis labels (from left to right) represent the nuclear disc, bar, bulge, thin disc, thick disc, and stellar halo. The dots represent the values of the best-fitting model, and the error bars indicate the 1σ confidence level.

2023), the star formation of the galaxy might have ceased due to strangulation-dominated environmental quenching (e.g. Morokuma-Matsui et al. 2022; Martig et al. 2026), which has led to an ancient ($t_{\rm bar} \sim 13$ Gyr and $t_{\rm bar,form} \sim 13$ Gyr) bar in the present day.

Theoretical studies have indicated that bars formed in rotation-dominated discs typically exhibit high pattern speeds during their early evolution, as demonstrated in simulations (e.g. Semczuk et al. 2024; Habibi et al. 2024). As shown in Fig. C.2, the dark matter in NGC 1381 becomes dominant at radii comparable to or smaller than the bar length. Therefore, dynamical friction between the bar and dark matter could transfer the bar's angular momentum to the dark matter halo (e.g. Tremaine & Weinberg 1984b; Weinberg 1985; Debattista & Sellwood 2000), significantly reducing the pattern speed, $\Omega_{\rm p}$. This scenario is also supported by studies of individual galaxies that contain slow bars (e.g. UGC 628, Chemin & Hernandez 2009; NGC 4277, Buttitta et al. 2022; NGC 4371, Tahmasebzadeh et al. 2024; NGC 6951, Lee et al. 2025). The effect of dynamical friction might have been enhanced after the galaxy's infall into the cluster, when the bar could no longer gain angular momentum from gas inflows. Furthermore, $\Omega(R)$ in NGC 1381's outer regions is mainly affected by dark matter, leading to an $R_{\rm CR}$ comparable to that of nearby massive galaxies despite the galaxy's lower stellar mass.

In practice, we cannot fully exclude the influence of model uncertainties on the rotation rate, $\mathcal{R}$, but our conclusion that the galaxy hosts a slow bar remains robust. The angular velocity profile, $\Omega(R)$, was well constrained in our modelling, as the observed kinematic maps were fully utilised to constrain the gravitational potential. The bar pattern speed, $\Omega_{\rm p}$, can be recovered with a relative uncertainty of $\lesssim$15%, as demonstrated in our previous simulation tests (Jin et al. 2025a). The dynamical bar length, $R_{\rm bar}$, is degenerate with the bar azimuthal angle, φ, since we observe only the projected bar (projected length $\sim R_{\rm bar} \sin|\varphi|$). Consequently, a smaller $|\varphi|$ leads to a longer inferred $R_{\rm bar}$. In this work, we derived $|\varphi| = 30^{+4}_{-14}{}^{\circ}$, corresponding to an end-on bar. The BP/X-shaped structure in the galaxy, as shown in Fig. 1, is difficult to detect from an extremely end-on view ($|\varphi| \lesssim 15°$), which indicates that the model-predicted $|\varphi|$ is unlikely to be overestimated and $R_{\rm bar}$ is unlikely to be underestimated. The robustness of $\Omega(R)$, $\Omega_{\rm p}$, and $R_{\rm bar}$ ensures the accuracy of the derived $\mathcal{R}$ in our analysis.

5.2. The assembly history of NGC 1381

We analysed the physical origins of different structures to investigate the assembly history of NGC 1381. The mean metallicities and [Mg/Fe] abundances shown in Fig. 12 demonstrate two distinct stellar populations in NGC 1381: (1) the metal-rich, α-poor, and old nuclear disc, bar, and thin disc; and (2) the metal-poor and α-rich bulge, thick disc, and stellar halo, which are younger than or comparable in age to the first group.

The stellar populations of the nuclear disc, bar, and thin disc, which are similarly metal-rich and α-poor, support their in situ origins. The bar likely formed through the dynamical reshaping of the thin disc, while the nuclear disc might be the result of in situ star formation from gas inflow driven by the bar or other clumpy instabilities (e.g. Neumayer et al. 2020). For NGC 1381, the bar-driven scenario is a reasonable explanation (e.g. Debattista et al. 2004; Athanassoula 2013) and would produce a dynamically cold nuclear disc at its early stage. We note that the nuclear disc at present is dynamically warm ($\overline{\lambda_z} = 0.57^{+0.12}_{-0.11}$), which might be caused by long-term dynamical heating from the bar, or simply by mixing with the dynamically hot bulge, given the relatively loose kinematic constraint we adopted ($\lambda_z > 0.5$; see Fig. 4).

In contrast, the metal-poor and α-rich stellar populations in the bulge, thick disc, and stellar halo may have either formed in situ at an early epoch through a rapid process – similar to the thick disc formation scenario proposed for the Milky Way (e.g. Lehnert et al. 2014; Helmi et al. 2018; Yu et al. 2021) – or have been accreted later via minor mergers. However, unlike in the Milky Way, the thin disc and bar in NGC 1381 are older than or comparable in age to the bulge, thick disc, and halo. The presence of the bar and the strangulation-dominated (rather than rapid) quenching of NGC 1381 (e.g. Morokuma-Matsui et al. 2022; Martig et al. 2026) indicate that the thin disc has experienced a sustained period of secular evolution and star formation. Therefore, early in situ components should be substantially older than the thin disc and bar; the observed age relationships do not support an early in situ origin for the bulge, thick disc, or halo.

We therefore suggest that a non-negligible fraction of the stars in the bulge, thick disc, and halo of NGC 1381 were accreted through minor mergers that occurred after the formation of the thin disc and bar. Their low metallicity and enhanced α-element abundances are consistent with an origin in lower-mass systems like dwarf galaxies. Moreover, the fact that these accretion events did not disrupt the pre-existing thin disc and bar further supports their interpretation as minor mergers.

The similarly old ages of all six components suggest that NGC 1381 may have fallen into the Fornax cluster early, consistent with previous works (e.g. Iodice et al. 2019b; Ding et al. 2023). The cluster environment has therefore influenced the galaxy's subsequent evolution. In addition to strangulation-dominated quenching, other processes such as dynamical

harassment or tidal interactions may have dynamically heated the galaxy's structures, especially the loosely bound outer regions. However, the clear difference in stellar populations between the thin and thick discs (see Fig. 12) argues against the scenario in which the thick disc was built through the dynamical heating of the thin disc. The similar radial extents of the thin and thick discs (see Figs. 7 and 8), together with the lack of obvious metallicity and [Mg/Fe] gradients in the thick disc (see Fig. 13), also argue against the outer regions of the thin disc having been transformed into thick disc stars via dynamical heating. Instead, the stellar population in the thick disc is highly similar to that in the halo, suggesting that their origins differ from that of the thin disc.

In Fig. 13, only the bulge shows a negative metallicity gradient ($\nabla[Z/H]_{\rm bulge} < 0$ for all data versions). The metallicity gradients of other components, as well as all [Mg/Fe] abundance gradients, are not significant. These results indicate that, apart from the bulge, stars in each component share similar stellar populations, suggesting similar physical origins (in situ for the bar, thin disc, and nuclear disc; ex situ for the thick disc and halo). In contrast, the bulge's negative gradient can arise either from the main galaxy or from the accreted dwarf galaxies; its precise origin remains ambiguous given the limitations of the current data. Due to this negative gradient and the uncertainties in stellar age, we cannot fully rule out the possibility of a primordial bulge predating the bar formation, nor can we quantify the ex situ fraction of the bulge.

Our findings are consistent with Pinna et al. (2019a), who defined the thick disc of NGC 1381 directly from the projected 2D image and attributed its origin to the accretion of ex situ stars. Compared to their results, our study performs a more physically motivated 3D decomposition, successfully distinguishing structures with different origins, particularly the bar, bulge, and nuclear disc. We further reveal that ex situ stars are present not only in the outer regions (thick disc and stellar halo) but also in the inner regions (bulge) of the galaxy.

Based on the analysis in this subsection and Sect. 5.1, we propose the following assembly history for NGC 1381: The galaxy likely formed its bar from a rotation-dominated disc approximately 13 Gyr ago. Then, the nuclear disc formed from gas inflow and/or radial migration of disc stars driven by the bar. The bar was fast initially but gradually slowed down due to dynamical friction with dark matter. The galaxy experienced a series of minor mergers, which built up its thick disc and stellar halo. These mergers also led to the formation (or growth) of the dynamically hot bulge. After the galaxy fell into the Fornax cluster 8–12 Gyr ago, the gas supply in the outer regions of the galaxy was cut off (strangulation), resulting in the galaxy being finally quenched but with its internal structures well preserved. This environmental quenching might have further enhanced the bar's slowdown by halting the supply of angular momentum, leading to a slow bar with $\mathcal{R} > 2$ at present.

6. Summary

We constructed 3D chemo-dynamical models for the barred S0 galaxy NGC 1381 in the Fornax cluster, using the barred population-orbit superposition method developed and validated in Jin et al. (2025a,b). We decomposed this galaxy into six components based on stellar orbits, namely a nuclear disc, a bar, a bulge, a thin disc, a thick disc, and a stellar halo. We analysed the stellar kinematics, luminosity distributions, and stellar populations of each component and inferred their physical origins. The main conclusions are as follows.

1. We decomposed NGC 1381 into six components with distinct kinematics and morphologies: (1) a dynamically warm nuclear disc ($f_{\rm nucl} = 4.8^{+3.9}_{-1.1}\%$); (2) a rigidly rotating, BP/X-shaped bar ($f_{\rm bar} = 30.2^{+2.3}_{-5.4}\%$); (3) a dynamically hot, spheroidal bulge ($f_{\rm bulge} = 17.1^{+5.0}_{-2.9}\%$); (4) a dynamically cold thin disc ($f_{\rm thin} = 27.5^{+2.2}_{-3.7}\%$); (5) a vertically extended thick disc with slightly slower rotation than the thin disc ($f_{\rm thick} = 15.5^{+1.2}_{-4.0}\%$); and (6) a dynamically hot, spatially diffuse stellar halo ($f_{\rm halo} = 4.9^{+3.5}_{-1.5}\%$).
2. Our modelling reveals the presence of a slow bar ($\mathcal{R} = 2.40^{+0.54}_{-0.27}$) in NGC 1381, with a bar pattern speed of $\Omega_{\rm p} = 34^{+4}_{-7}\,{\rm km\,s^{-1}\,kpc^{-1}}$, a bar length of $R_{\rm bar} = 2.24^{+0.43}_{-0.22}$ kpc, and a corotation radius of $R_{\rm CR} = 5.38^{+1.59}_{-0.28}$ kpc.
3. The stellar metallicities and [Mg/Fe] abundances exhibit clear differences between components: The nuclear disc, bar, and thin disc are metal-rich ($[Z/H] \gtrsim 0$ for versions A and B; $[Z/H] \gtrsim -0.3$ for version C) and α-poor ($[{\rm Mg/Fe}] \lesssim 0.2$ for versions A and B; $[{\rm Mg/Fe}] \lesssim 0.25$ for version C), while the bulge, thick disc, and stellar halo are metal-poor ($[Z/H] \lesssim 0$ for versions A and B; $[Z/H] \lesssim -0.3$ for version C) and α-rich ($[{\rm Mg/Fe}] \gtrsim 0.2$ for versions A and B; $[{\rm Mg/Fe}] \gtrsim 0.25$ for version C). The bulge shows a negative metallicity gradient ($\nabla[Z/H]_{\rm bulge} < 0$), while the metallicity gradients of other components and the [Mg/Fe] abundance gradients of all components are not significant. All components in NGC 1381 are generally old (8–14 Gyr). Compared to the nuclear disc, bar, and thin disc, the bulge, thick disc, and stellar halo are either younger or of comparable age.

Based on these results, we infer that the nuclear disc, bar, and thin disc of NGC 1381 formed in situ in the early Universe. The bar was likely fast initially but gradually slowed due to dynamical friction with the dark matter halo and the lack of gas supply after the galaxy's infall into the cluster. In contrast, the thick disc and stellar halo likely formed via minor mergers. These mergers also contributed to the formation or growth of the dynamically hot bulge.

As a fossil record from the early Universe, NGC 1381 provides valuable insights into early galaxy evolution. This particular galaxy serves as a non-trivial local descendant of the barred galaxies at $z \gtrsim 2$ discovered by JWST observations (e.g. Le Conte et al. 2024; Guo et al. 2025). A valuable next step will be to statistically study barred galaxies in both cluster and non-cluster environments and to compare them with future IFS observations of high-redshift galaxies. Such a comparative analysis will advance our understanding of the evolution of barred galaxies from high redshifts to the present day.

Acknowledgements. We thank Dr. Richard J. Long for useful discussions. This work is supported by the National Natural Science Foundation of China under Grant No. 12403017. This work is partly supported by the National Natural Science Foundation of China (Grant No. 11821303 to SM) and the CAS Project for Young Scientists in Basic Research, Grant No. YSBR-062 (LZ). FP acknowledges support from the Horizon Europe research and innovation programme under the Maria Skłodowska-Curie grant 'TraNSLate' No. 101108180.

References

Aguerri, J. A. L., Méndez-Abreu, J., Falcón-Barroso, J., et al. 2015, A&A, 576, A102
Athanassoula, E. 1992a, MNRAS, 259, 345
Athanassoula, E. 1992b, MNRAS, 259, 328
Athanassoula, E. 2003, MNRAS, 341, 1179
Athanassoula, E. 2005, MNRAS, 358, 1477
Athanassoula, E. 2013, in Secular Evolution of Galaxies, eds. J. Falcón-Barroso, & J. H. Knapen, 305
Bacon, R., Copin, Y., Monnet, G., et al. 2001, MNRAS, 326, 23
Bacon, R., Accardo, M., Adjali, L., et al. 2010, SPIE Conf. Ser., 7735, 773508

Bacon, R., Conseil, S., Mary, D., et al. 2017, A&A, 608, A1
Barnabè, M., Dutton, A. A., Marshall, P. J., et al. 2012, MNRAS, 423, 1073
Binney, J., & Tremaine, S. 2008, Galactic Dynamics: Second Edition (Princeton University Press)
Blakeslee, J. P., Jordán, A., Mei, S., et al. 2009, ApJ, 694, 556
Bournaud, F., Elmegreen, B. G., & Elmegreen, D. M. 2007, ApJ, 670, 237
Breda, I., Papaderos, P., & Gomes, J.-M. 2020, A&A, 640, A20
Bryant, J. J., Owers, M. S., Robotham, A. S. G., et al. 2015, MNRAS, 447, 2857
Bundy, K., Bershady, M. A., Law, D. R., et al. 2015, ApJ, 798, 7
Bureau, M., & Athanassoula, E. 2005, ApJ, 626, 159
Bureau, M., Aronica, G., Athanassoula, E., et al. 2006, MNRAS, 370, 753
Buta, R. J., & Zhang, X. 2009, ApJS, 182, 559
Buta, R. J., Sheth, K., Athanassoula, E., et al. 2015, ApJS, 217, 32
Buttitta, C., Corsini, E. M., Cuomo, V., et al. 2022, A&A, 664, L10
Cappellari, M. 2002, MNRAS, 333, 400
Cappellari, M. 2017, MNRAS, 466, 798
Cappellari, M., & Copin, Y. 2003, MNRAS, 342, 345
Cappellari, M., & Emsellem, E. 2004, PASP, 116, 138
Cappellari, M., Emsellem, E., Krajnović, D., et al. 2011, MNRAS, 413, 813
Cappellari, M., Scott, N., Alatalo, K., et al. 2013, MNRAS, 432, 1709
Chemin, L., & Hernandez, O. 2009, A&A, 499, L25
Chung, A., & Bureau, M. 2004, AJ, 127, 3192
Contopoulos, G., & Mertzanides, C. 1977, A&A, 61, 477
Cristiani, V. A., Abadi, M. G., Taverna, A., et al. 2024, A&A, 692, A63
Cuomo, V., Aguerri, J. A. L., Corsini, E. M., & Debattista, V. P. 2020, A&A, 641, A111
Dattathri, S., Valluri, M., Vasiliev, E., Wheeler, V., & Erwin, P. 2024, MNRAS, 530, 1195
de Sá-Freitas, C., Fragkoudi, F., Gadotti, D. A., et al. 2023, A&A, 671, A8
de Sá-Freitas, C., Gadotti, D. A., Fragkoudi, F., et al. 2025, A&A, 698, A5
Debattista, V. P., & Sellwood, J. A. 2000, ApJ, 543, 704
Debattista, V. P., Carollo, C. M., Mayer, L., & Moore, B. 2004, ApJ, 604, L93
Ding, Y., Zhu, L., van de Ven, G., et al. 2023, A&A, 672, A84
Drinkwater, M. J., Gregg, M. D., & Colless, M. 2001, ApJ, 548, L139
Du, M., Ho, L. C., Zhao, D., et al. 2019, ApJ, 884, 129
Du, M., Ho, L. C., Debattista, V. P., et al. 2020, ApJ, 895, 139
Du, M., Ho, L. C., Debattista, V. P., et al. 2021, ApJ, 919, 135
Efstathiou, G., Lake, G., & Negroponte, J. 1982, MNRAS, 199, 1069
Emsellem, E., Monnet, G., & Bacon, R. 1994, A&A, 285, 723
Erwin, P., & Debattista, V. P. 2017, MNRAS, 468, 2058
Erwin, P., Seth, A., Debattista, V. P., et al. 2021, MNRAS, 502, 2446
Ferguson, H. C. 1989, AJ, 98, 367
Fisher, D. B., & Drory, N. 2008, AJ, 136, 773
Fraser-McKelvie, A., van de Sande, J., Gadotti, D. A., et al. 2025, A&A, 700, A237
Gadotti, D. A. 2009, MNRAS, 393, 1531
Gadotti, D. A. 2011, MNRAS, 415, 3308
Gadotti, D. A. 2026, MNRAS, 545, staf2072
Gadotti, D. A., Bittner, A., Falcón-Barroso, J., et al. 2020, A&A, 643, A14
Garma-Oehmichen, L., Hernández-Toledo, H., Aquino-Ortíz, E., et al. 2022, MNRAS, 517, 5660
Gerhard, O. E. 1993, MNRAS, 265, 213
Grand, R. J. J., Gómez, F. A., Marinacci, F., et al. 2017, MNRAS, 467, 179
Grand, R. J. J., Fragkoudi, F., Gómez, F. A., et al. 2024, MNRAS, 532, 1814
Guo, R., Mao, S., Athanassoula, E., et al. 2019, MNRAS, 482, 1733
Guo, Y., Jogee, S., Wise, E., et al. 2025, ApJ, 985, 181
Habibi, A., Roshan, M., Hosseinirad, M., et al. 2024, A&A, 691, A122
Helmi, A., Babusiaux, C., Koppelman, H. H., et al. 2018, Nature, 563, 85
Hohl, F. 1971, ApJ, 168, 343
Hopkins, P. F., Bundy, K., Croton, D., et al. 2010, ApJ, 715, 202
Iodice, E., Capaccioli, M., Grado, A., et al. 2016, ApJ, 820, 42
Iodice, E., Spavone, M., Capaccioli, M., et al. 2019a, A&A, 623, A1
Iodice, E., Sarzi, M., Bittner, A., et al. 2019b, A&A, 627, A136
Jethwa, P., Thater, S., Maindl, T., & Van de Ven, G. 2020, Astrophysics Source Code Library [record ascl:2011.007]
Jin, Y., Zhu, L., Long, R. J., et al. 2019, MNRAS, 486, 4753
Jin, Y., Zhu, L., Long, R. J., et al. 2020, MNRAS, 491, 1690
Jin, Y., Zhu, L., Zibetti, S., et al. 2024, A&A, 681, A95
Jin, Y., Zhu, L., Tahmasebzadeh, B., et al. 2025a, A&A, 700, A249
Jin, Y., Zhu, L., Tahmasebzadeh, B., et al. 2025b, A&A, 704, A262
Kormendy, J., & Kennicutt, R. C., Jr. 2004, ARA&A, 42, 603
Kroupa, P. 2001, MNRAS, 322, 231
Lawson, C. L., & Hanson, R. J. 1974, Solving Least Squares Problems (Englewood Cliffs: Prentice-Hall)
Le Conte, Z. A., Gadotti, D. A., Ferreira, L., et al. 2024, MNRAS, 530, 1984
Lee, Y. H., Hwang, H. S., Cuomo, V., et al. 2025, ApJ, 989, 55
Lehnert, M. D., Di Matteo, P., Haywood, M., & Snaith, O. N. 2014, ApJ, 789, L30
Li, Z.-Y., Ho, L. C., & Barth, A. J. 2017, ApJ, 845, 87
Li, Z.-Y., Shen, J., Bureau, M., et al. 2018, ApJ, 854, 65
Łokas, E. L. 2018, ApJ, 857, 6
Long, R. J., & Mao, S. 2018, Res. Astron. Astrophys., 18, 145
Lütticke, R., Dettmar, R. J., & Pohlen, M. 2000, A&AS, 145, 405
Martig, M., Pinna, F., Falcón-Barroso, J., et al. 2021, MNRAS, 508, 2458
Martig, M., Pinna, F., Falcón-Barroso, J., et al. 2026, MNRAS, 547, stag458
Martín-Navarro, I., Pinna, F., Coccato, L., et al. 2021, A&A, 654, A59
Méndez-Abreu, J., Ruiz-Lara, T., Sánchez-Menguiano, L., et al. 2017, A&A, 598, A32
Molaeinezhad, A., Falcón-Barroso, J., Martínez-Valpuesta, I., et al. 2016, MNRAS, 456, 692
Morokuma-Matsui, K., Bekki, K., Wang, J., et al. 2022, ApJS, 263, 40
Navarro, J. F., Frenk, C. S., & White, S. D. M. 1996, ApJ, 462, 563
Neumayer, N., Seth, A., & Böker, T. 2020, A&ARv, 28, 4
Neureiter, B., Thomas, J., Saglia, R., et al. 2021, MNRAS, 500, 1437
Noguchi, M. 1996, ApJ, 469, 605
Ortega-Martinez, S., Obreja, A., Dominguez-Tenreiro, R., et al. 2022, MNRAS, 516, 197
Ostriker, J. P., & Peebles, P. J. E. 1973, ApJ, 186, 467
Pietrinferni, A., Cassisi, S., Salaris, M., & Castelli, F. 2004, ApJ, 612, 168
Pietrinferni, A., Cassisi, S., Salaris, M., & Castelli, F. 2006, ApJ, 642, 797
Pinna, F., Falcón-Barroso, J., Martig, M., et al. 2019a, A&A, 623, A19
Pinna, F., Falcón-Barroso, J., Martig, M., et al. 2019b, A&A, 625, A95
Poci, A., McDermid, R. M., Zhu, L., & van de Ven, G. 2019, MNRAS, 487, 3776
Poci, A., McDermid, R. M., Lyubenova, M., et al. 2021, A&A, 647, A145
Pulsoni, C., Gerhard, O., Arnaboldi, M., et al. 2020, A&A, 641, A60
Quenneville, M. E., Liepold, C. M., & Ma, C.-P. 2022, ApJ, 926, 30
Rautiainen, P., Salo, H., & Laurikainen, E. 2008, MNRAS, 388, 1803
Rix, H.-W., de Zeeuw, P. T., Cretton, N., van der Marel, R. P., & Carollo, C. M. 1997, ApJ, 488, 702
Ruiz-García, M., Querejeta, M., García-Burillo, S., et al. 2024, A&A, 691, A351
Sánchez, S. F., Kennicutt, R. C., Gil de Paz, A., et al. 2012, A&A, 538, A8
Sánchez-Blázquez, P., Peletier, R. F., Jiménez-Vicente, J., et al. 2006, MNRAS, 371, 703
Santucci, G., Brough, S., van de Sande, J., et al. 2022, ApJ, 930, 153
Santucci, G., Brough, S., van de Sande, J., et al. 2023, MNRAS, 521, 2671
Sarzi, M., Iodice, E., Coccato, L., et al. 2018, A&A, 616, A121
Sattler, N., Pinna, F., Neumayer, N., et al. 2023, MNRAS, 520, 3066
Sattler, N., Pinna, F., Comerón, S., et al. 2025, A&A, 698, A235
Schwarzschild, M. 1979, ApJ, 232, 236
Schwarzschild, M. 1982, ApJ, 263, 599
Schwarzschild, M. 1993, ApJ, 409, 563
Semczuk, M., Dehnen, W., Schönrich, R., & Athanassoula, E. 2024, A&A, 692, A159
Sersic, J. L. 1968, Atlas de Galaxias Australes (Argentina: Observatorio Astronomico)
Shaw, M. A. 1987, MNRAS, 229, 691
Spriggs, T. W., Sarzi, M., Galán-de Anta, P. M., et al. 2021, A&A, 653, A167
Tahmasebzadeh, B., Zhu, L., Shen, J., Gerhard, O., & Qin, Y. 2021, MNRAS, 508, 6209
Tahmasebzadeh, B., Zhu, L., Shen, J., Gerhard, O., & van de Ven, G. 2022, ApJ, 941, 109
Tahmasebzadeh, B., Zhu, L., Shen, J., et al. 2024, MNRAS, 534, 861
Thater, S., Jethwa, P., Lilley, E. J., et al. 2025, IAU Symp., 379, 314
Tremaine, S., & Weinberg, M. D. 1984b, MNRAS, 209, 729
van de Ven, G., Falcón-Barroso, J., & Lyubenova, M. 2025, ARA&A, 63, 259
van den Bosch, R. C. E., van de Ven, G., Verolme, E. K., Cappellari, M., & de Zeeuw, P. T. 2008, MNRAS, 385, 647
van der Marel, R. P., & Franx, M. 1993, ApJ, 407, 525
Vasiliev, E., & Valluri, M. 2020, ApJ, 889, 39
Vazdekis, A., Sánchez-Blázquez, P., Falcón-Barroso, J., et al. 2010, MNRAS, 404, 1639
Vazdekis, A., Coelho, P., Cassisi, S., et al. 2015, MNRAS, 449, 1177
Venhola, A., Peletier, R., Laurikainen, E., et al. 2018, A&A, 620, A165
Weinberg, M. D. 1985, MNRAS, 213, 451
Wu, X., Zhu, L., Chang, J., Zeng, G., & Lei, Y. 2025, A&A, 699, A374
Yoon, Y., Im, M., Lee, G.-H., Lee, S.-K., & Lim, G. 2019, Nat. Astron., 3, 844
Yu, S., Bullock, J. S., Klein, C., et al. 2021, MNRAS, 505, 889
Zana, T., Lupi, A., Bonetti, M., et al. 2022, MNRAS, 515, 1524
Zhao, H. 1996, MNRAS, 278, 488
Zhu, L., van den Bosch, R., van de Ven, G., et al. 2018a, MNRAS, 473, 3000
Zhu, L., van de Ven, G., van den Bosch, R., et al. 2018b, Nat. Astron., 2, 233
Zhu, L., van de Ven, G., Méndez-Abreu, J., & Obreja, A. 2018c, MNRAS, 479, 945
Zhu, L., van de Ven, G., Leaman, R., et al. 2020, MNRAS, 496, 1579
Zhu, L., Pillepich, A., van de Ven, G., et al. 2022a, A&A, 660, A20
Zhu, L., van de Ven, G., Leaman, R., et al. 2022b, A&A, 664, A115

Appendix A: Stellar population maps for data versions B and C

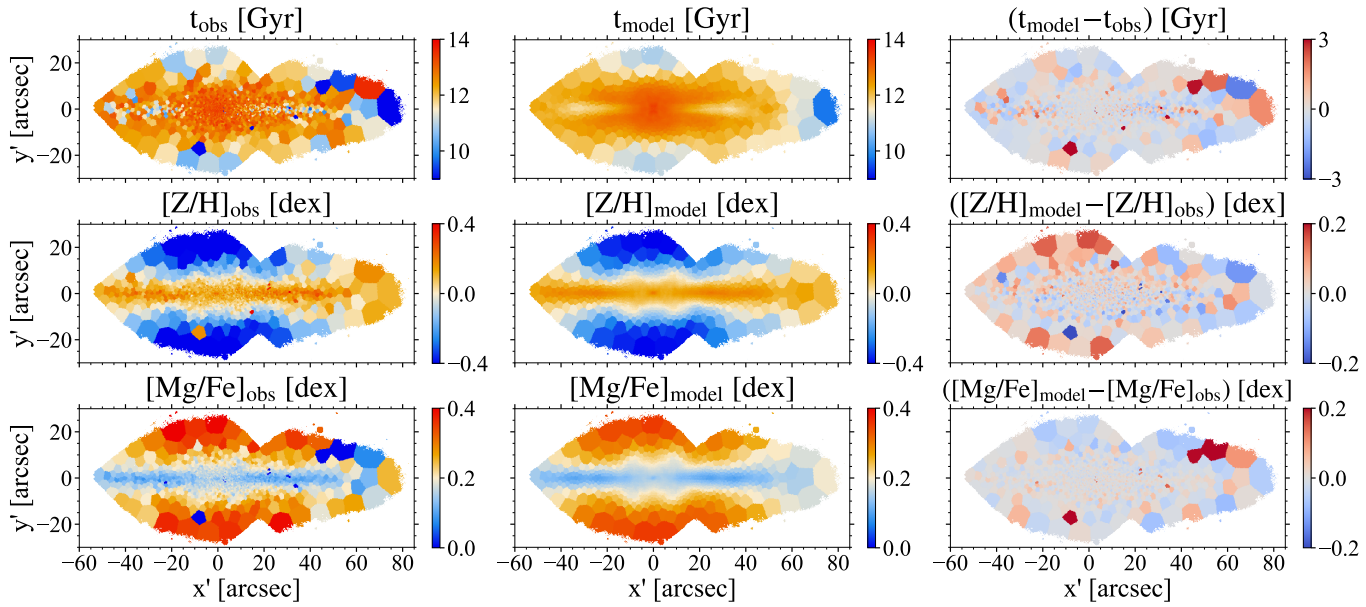


Fig. A.1. Same as the bottom three panels of Fig. 3 but for data version B.

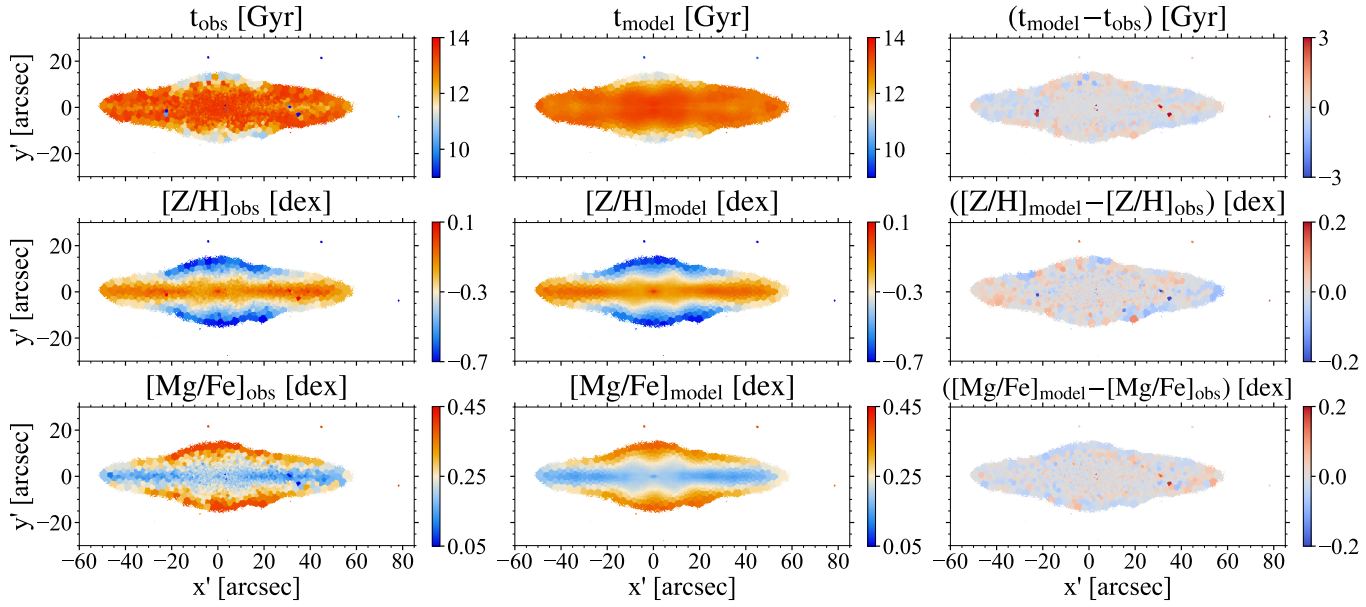


Fig. A.2. Same as the bottom three panels of Fig. 3 but for data version C.

The stellar population data and model fittings based on data version B (Pinna et al. 2019a) are shown in Fig. A.1, while those from version C (Martín-Navarro et al. 2021) are presented in Fig. A.2. Compared to versions A and B, version C has systematic offsets in the stellar metallicity and [Mg/Fe] abundance, which originate from their different settings when fitting the spectra. Nevertheless, the overall trends in the maps are consistent, ensuring the robustness of our main conclusions.

Appendix B: MGE fitting results

The r-band surface brightness of NGC 1381 was fitted by the MGE formalism (Cappellari 2002), which can be expressed as

$$\Sigma(x', y') = \sum_{j=1}^{N} \frac{L_j}{2\pi\sigma_j'^2 q_j'} \exp\left[-\frac{1}{2\sigma_j'^2}\left(x'^2 + \frac{y'^2}{q_j'^2}\right)\right], \tag{B.1}$$

Table B.1. MGE fitting parameters for NGC 1381.

Component	L_j [$L_\odot$]	σ'_j [arcsec]	q'_j
Triaxial bar	5.8514e+09	0.6156	0.9399
	2.3452e+09	0.8111	0.2924
	4.8630e+09	1.5880	0.8384
	4.9462e+09	3.6569	0.5827
	-2.8594e+09	4.4236	0.4186
	1.0836e+09	6.9692	0.5614
	4.5652e+08	7.9081	0.8153
Axisymmetric disc	7.9384e+08	13.8476	0.1330
	4.7452e+08	16.0688	0.5392
	-1.9755e+10	17.3858	0.1379
	1.9177e+10	17.8108	0.1352
	1.6929e+07	19.4488	0.9399
	-1.0310e+09	20.1765	0.3888
	7.9930e+08	23.5237	0.2900
	7.5981e+07	38.0095	0.2818
	8.7859e+06	58.4657	0.6147

Notes. From left to right: (1) the component to which each Gaussian belongs; (2) luminosity L_j; (3) dispersion σ'_j; (4) axis ratio q'_j. These MGE parameters were calculated from Eq. (B.1).

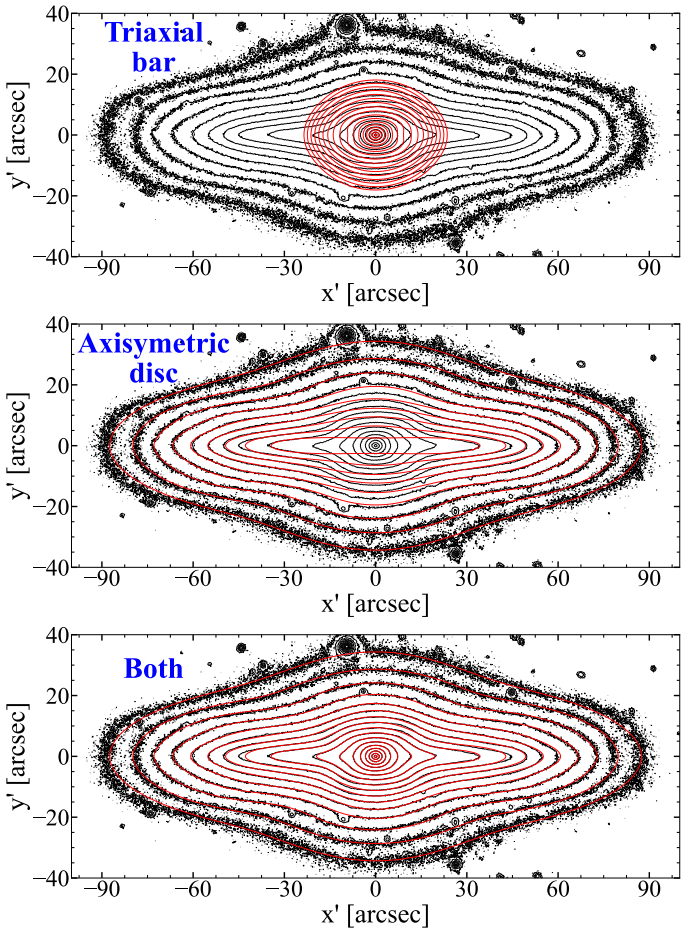


Fig. B.1. Observed surface brightness contours (black) and MGE-fitted contours (red) for NGC 1381. The red contours represent the triaxial bar component, the axisymmetric disc component, and the sum of the two components in the MGE fitting results, respectively (see Table B.1). The contour interval is 0.5 magnitude.

where N is the number of Gaussians, the subscript j denotes the j-th Gaussian, L_j is the total luminosity, $q'_j = b'_j/a'_j$ is the axis ratio, and σ'_j is the dispersion along the major axis x'. Negative Gaussians are allowed ($L_j < 0$) in order to fit the BP/X-shaped structure. The fitted MGE parameters are listed in Table B.1, with the corresponding surface brightness contours shown in Fig. B.1.

Appendix C: Parameter space and mass profiles

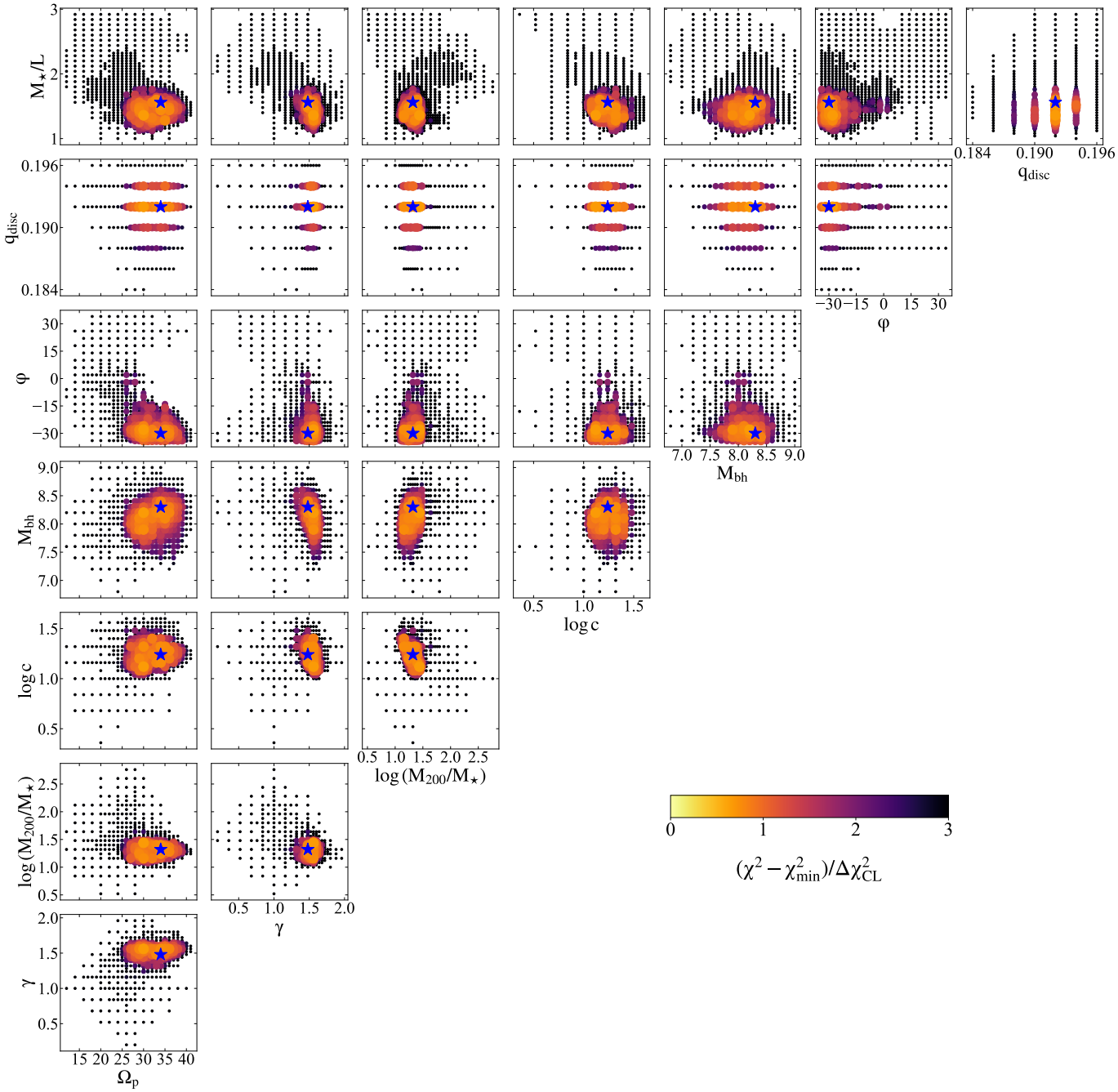


Fig. C.1. Parameter space we explored for NGC 1381. The eight free parameters are the disc axis ratio, $q_{\rm disc}$ (transformed from the inclination angle, θ); the bar azimuthal angle, φ; the stellar mass-to-light ratio, $M_\star/L$; the bar pattern speed, $\Omega_{\rm p}$; the dark matter concentration, c; the virial mass, M_{200}; the inner density slope of dark matter, γ; and the black hole mass, $M_{\rm BH}$. The blue star marks the best-fitting model with minimum χ^2 ($\chi^2_{\rm min}$), and the coloured dots indicate models that fall within the 3σ confidence level, with their χ^2 values indicated by the colour bar. The small black dots correspond to models outside the 3σ confidence level. For formal definitions of χ^2 and confidence levels, see Sects. 3.1 and 3.4.

The parameter space explored in our dynamical modelling is presented in Fig. C.1. The derived values of the free parameters are: (1) a disc axis ratio of $q_{\rm disc} = 0.192^{+0.002}_{-0.002}$ (corresponding to an inclination angle of $\theta \approx 87$–$88°$); (2) a bar azimuthal angle of $|\varphi| = 30^{+4}_{-14}{}^{\circ}$; (3) a stellar mass-to-light ratio of $M_\star/L = 1.56^{+0.12}_{-0.36}$ (corresponding to a stellar mass of $M_\star = 1.65^{+0.13}_{-0.38} \times 10^{10}\,{\rm M}_\odot$); (4) a bar pattern speed of $\Omega_{\rm p} = 34^{+4}_{-7}\,{\rm km\,s^{-1}\,kpc^{-1}}$; (5) a dark matter concentration of $\log c = 1.24^{+0.16}_{-0.16}$; (6) a virial mass of $M_{200} = 3.45^{+0.91}_{-1.55} \times 10^{11}\,{\rm M}_\odot$; (7) a dark matter inner density slope of $\gamma = 1.48^{+0.16}_{-0.04}$; and (8) a black hole mass of $M_{\rm BH} = 2.0^{+1.2}_{-1.5} \times 10^8\,{\rm M}_\odot$.

In our dynamical modelling, the gravitational potential comprises contributions from stellar mass, dark matter, and a supermassive black hole. This leads to a degeneracy between these three components, especially in the innermost regions ($\lesssim 5$ arcsec). Martín-Navarro et al. (2021) reported that the IMF becomes more bottom-heavy towards the innermost regions, leading to a higher

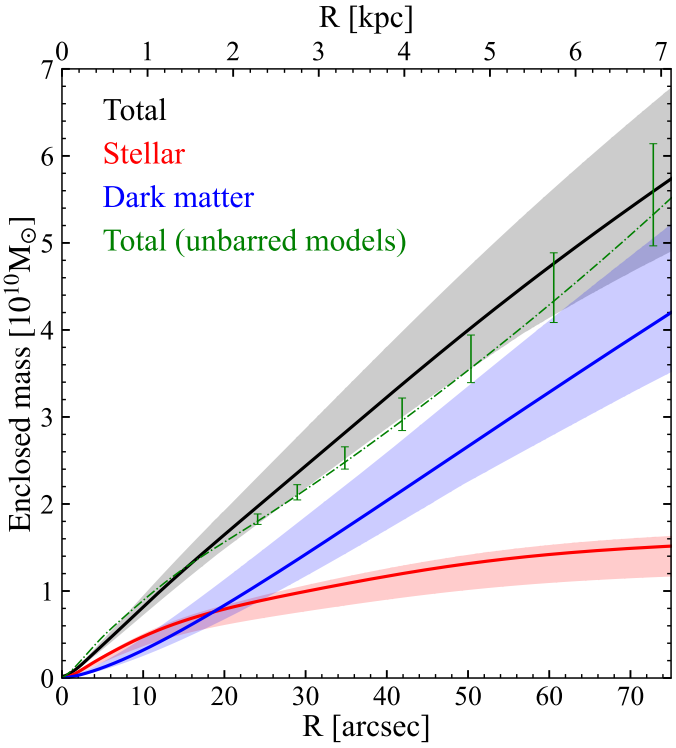


Fig. C.2. Enclosed mass profiles for NGC 1381. The black, red, and blue solid lines represent the profiles of total mass, stellar mass, and dark matter mass from the best-fitting model, respectively, while the shaded regions denote the model uncertainties within the 1σ confidence level. The green dashed line with error bars corresponds to the total mass profile from orbit-superposition models without considering the bar (Ding et al. 2023).

$M_\star/L$ there. Therefore, assuming a constant $M_\star/L$ likely results in an underestimation of the stellar mass in the central regions. However, this bias could be masked by models that adopt a more cuspy dark matter halo and/or a more massive black hole.

The enclosed stellar, dark matter, and total mass profiles are shown in Fig. C.2. We compared our total mass profile with the result from Ding et al. (2023), who constructed orbit-superposition models without considering the bar. Regardless of whether the bar is included in the models, the total mass profiles, which are directly constrained by the kinematic data, are consistent.

Appendix D: Circularity, λ_z: Definitions with and without cross terms in $V_{\rm rms}$

In this work, we adopted the circularity (λ_z) defined in Eq. (2) following previous works on orbit-superposition models (e.g. Zhu et al. 2018a; Tahmasebzadeh et al. 2022; Jin et al. 2025a). This definition of λ_z employs a root-mean-square velocity that includes cross terms ($\overline{V_{\rm rms}} = \sqrt{\overline{v_{x0}^2 + v_{y0}^2 + v_z^2 + 2v_{x0}v_{y0} + 2v_{x0}v_z + 2v_{y0}v_z}}$). For comparison, we also considered an alternative definition that excludes these cross terms ($\overline{V_{\rm rms,nocross}} = \sqrt{\overline{v_{x0}^2 + v_{y0}^2 + v_z^2}}$). The corresponding circularity is then written as

$$\lambda_{z,\rm nocross} = \overline{L_z}/(R \times \overline{V_{\rm rms,nocross}}). \tag{D.1}$$

Figure D.1 presents a one-to-one comparison of the circularity for each orbit in the best-fitting model under two definitions: λ_z and $\lambda_{z,\rm nocross}$. For most orbits, the two circularities have very similar values, especially for orbits with $\lambda_z > 0$. Only a small fraction of orbits, which account for 0.4% of all orbits and contribute 0.1% of the total luminosity, have a difference of $|\lambda_z - \lambda_{z,\rm nocross}| \geq 0.05$. Since the orbit classification criteria we adopted use a threshold of $\lambda_z = 0.5$ (see Fig. 4), the definition of circularity does not affect our dynamical decompositions.

Appendix E: Stellar orbit distributions in the λ_z–$E_{\rm bind}$ phase space

As mentioned in Sect. 3.2, we adopted the bar length ($R_{\rm bar}$) to separate the inner components (nuclear disc, bar, and bulge) from the outer components (thin disc, thick disc, and stellar halo) of the galaxy. The reasons for this classification are as follows. First, the bar redistributes angular momentum within $R_{\rm bar}$; for example, there is a lack of dynamically cold orbits at $\sim$ 1.5 kpc (see Fig. 5), which clearly separates the inner (nuclear) disc from the outer (thin and thick) discs. Second, the time-averaged radius is highly correlated with the orbital binding energy. Therefore, for dynamically hot components, using a radius criterion is similar to using a binding-energy criterion. Fig. E.1 illustrates this: the separation in normalised binding energy ($\varepsilon = E_{\rm bind}/|E_{\rm min}| = -0.46$) is generally consistent with that based on $R_{\rm bar}$.

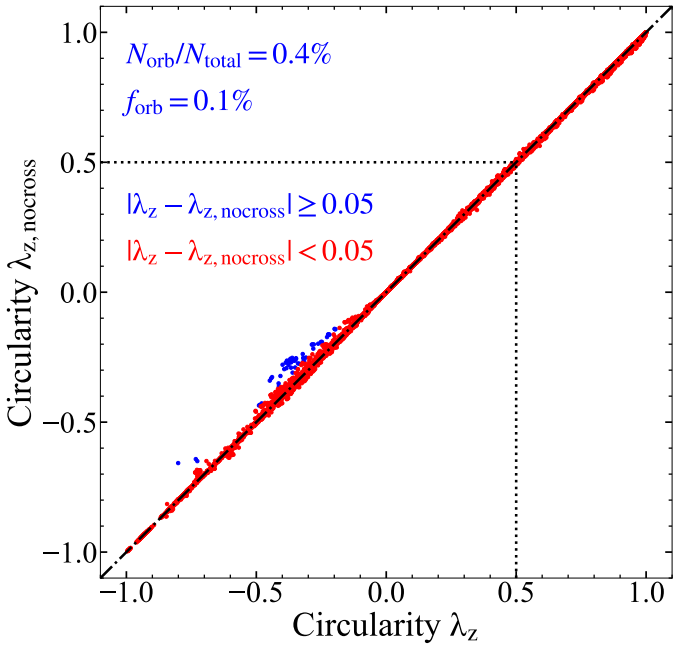


Fig. D.1. One-to-one comparison of the circularity for each orbit under two definitions. The default circularity λ_z adopted in this work (Eq. 2) is defined using the $V_{\rm rms}$ containing cross terms, while $\lambda_{z,\rm nocross}$ (Eq. D.1) is based on the $V_{\rm rms,nocross}$ where cross terms are excluded. Each orbit is represented by a dot. Red (blue) dots indicate orbits with $|\lambda_z - \lambda_{z,\rm nocross}| < 0.05$ (≥ 0.05). The orbits with $|\lambda_z - \lambda_{z,\rm nocross}| \geq 0.05$ only account for 0.4% of all orbits and contribute 0.1% of the total luminosity. The dashed line represents equality between the two definitions, and the dotted lines correspond to $\lambda_z = 0.5$ and $\lambda_{z,\rm nocross} = 0.5$.

Furthermore, we did not find an obvious bimodal distribution of dynamically hot orbits in the λ_z–$E_{\rm bind}$ plane, so it is hard to derive a distribution-based classification as Du et al. (2019, 2020) did. Using a fixed value to separate the different components is therefore a reasonable choice, and the value of $R_{\rm bar} = 2.24^{+0.43}_{-0.22}$ kpc is generally consistent with the physical scale of dynamical bulges ($\sim$ 2–3.5 kpc) found in simulations (e.g. Du et al. 2020, 2021) and adopted in previous dynamical models (e.g. Zhu et al. 2022a,b; Wu et al. 2025). Since the bulge and halo have similar metallicities and [Mg/Fe] abundances, using a separating radius different from $R_{\rm bar}$ will not affect our main conclusion that both the bulge and halo are likely related to early minor mergers.

Appendix F: Stellar orbit distributions in the λ_z–R phase space for barred and unbarred models

Figure F.1 shows a comparison between the stellar orbit distributions derived from the barred (this work) and unbarred (Ding et al. 2023) models. Since Ding et al. (2023) did not analyse the orbital morphological parameters ($p_{\rm orb}$, $q_{\rm orb,0}$, and $z_{\rm orb}$) adopted in this work, we directly compared different components using only the criteria based on λ_z and R.

In the galaxy's outer regions ($R > R_{\rm bar}$), the results from the barred and unbarred models are generally consistent: cold orbits ($\lambda_z \geq 0.8$) dominate, while warm ($0.25 < \lambda_z < 0.8$) and hot ($\lambda_z \leq 0.25$) orbits account for moderate and small fractions, respectively. For each component, the fraction is slightly lower in the unbarred model than in the barred model.

In the galaxy's inner regions ($R \leq R_{\rm bar}$), the unbarred model cannot reproduce the dynamical signature of a rigidly rotating bar (the strong λ_z–R correlation), resulting in a mixture of bar and bulge orbits. Nevertheless, the fractions of cold, warm, and hot orbits remain generally consistent, with the unbarred model yielding slightly higher fractions than the barred model.

Appendix G: Spatial distributions of mean velocity and velocity dispersion

Using the orbital information from the best-fitting model, we derived the 3D spatial distributions of luminosity-weighted mean velocity and velocity dispersion for each decomposed component. We then projected them onto the x-z plane and presented the resulting 2D distributions in Fig. G.1. The bulge and stellar halo are dominated by random motions, while the other components are dominated by rotation.

Appendix H: Stellar metallicity and [Mg/Fe] abundance profiles

Using the orbital information from the best-fitting model, we calculated the luminosity-weighted stellar metallicity and [Mg/Fe] abundance profiles and presented them in Fig. H.1. For the best-fitting model, the bulge exhibits a negative metallicity gradient and a positive [Mg/Fe] gradient, while the gradients of other components are not significant.

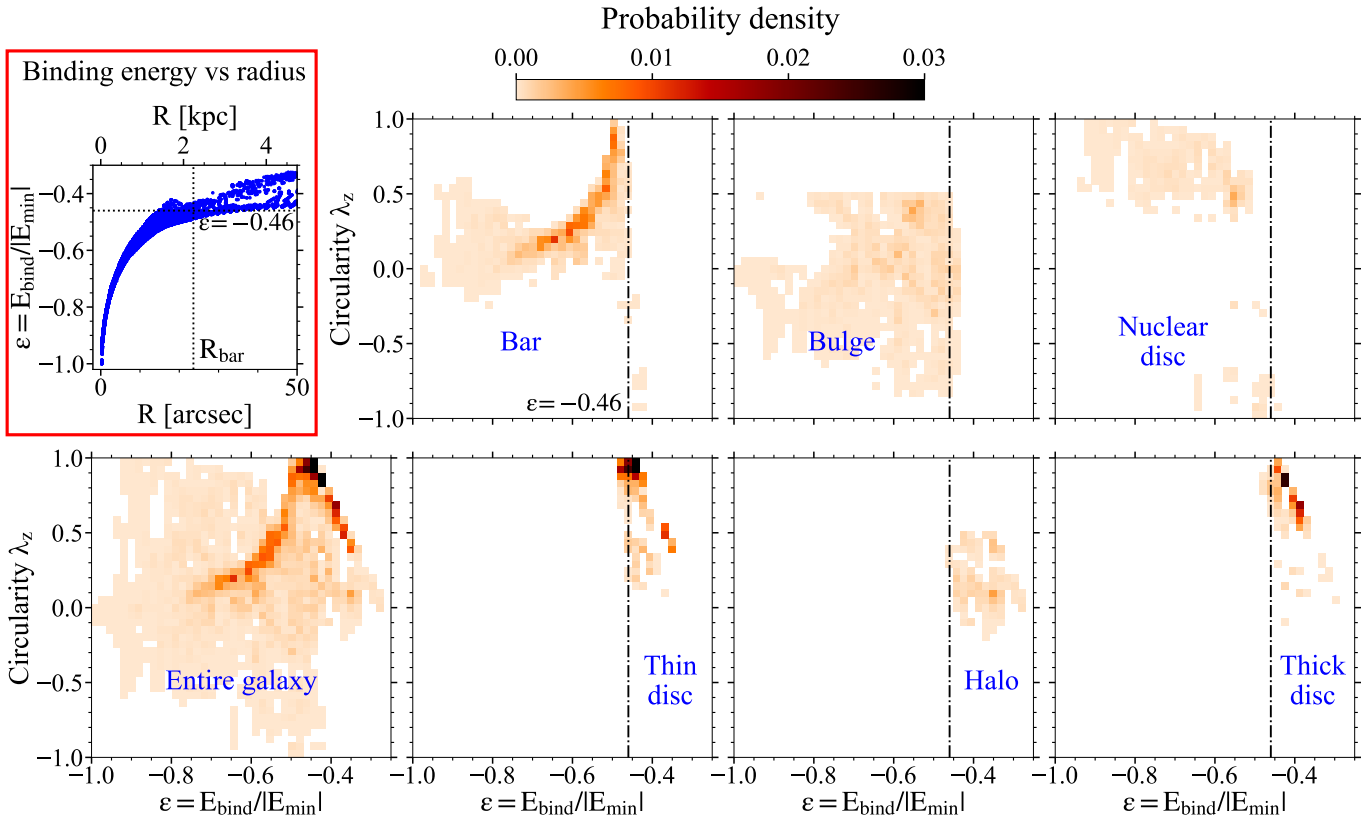


Fig. E.1. Probability density distributions of stellar orbits in the λ_z–$E_{\rm bind}$ phase space for the best-fitting model of NGC 1381. *Top left*: Relation between the orbital binding energy ($E_{\rm bind}$, normalised by its minimum value over all orbits in the model) and the time-averaged radius (R), with each orbit represented by a blue dot. The vertical dotted line represents the bar length ($R_{\rm bar}$), which is adopted to separate the inner components (nuclear disc, bar, and bulge) from the outer components (thin disc, thick disc, and stellar halo) of the galaxy. The horizontal dotted line indicates the average binding energy ($\varepsilon = E_{\rm bind}/|E_{\rm min}| = -0.46$) at $R_{\rm bar}$. *Other panels*: Stellar orbit distributions of the entire galaxy and of each dynamical component, corresponding to Fig. 5 but with the x-axis changed from radius (R) to normalised binding energy ($\varepsilon = E_{\rm bind}/|E_{\rm min}|$). The vertical dashed line represents $\varepsilon = -0.46$.

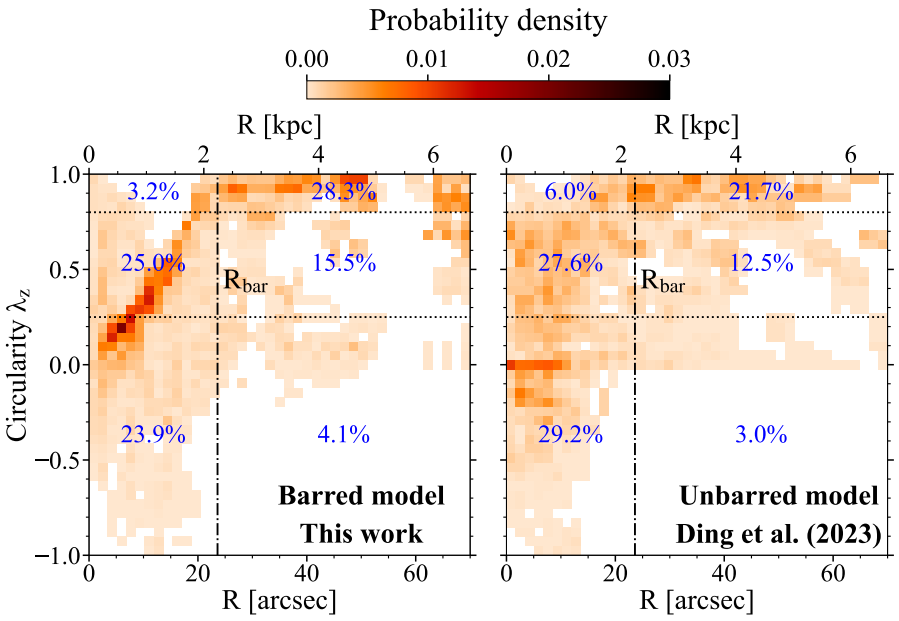


Fig. F.1. Probability density distributions of stellar orbits in the λ_z–R phase space for the best-fitting barred (*left*; this work) and unbarred (*right*; Ding et al. 2023) models of NGC 1381. The vertical dashed lines represent the dynamical bar length ($R_{\rm bar} = 2.24$ kpc), which separates the orbits in the galaxy's inner ($R \leq R_{\rm bar}$) and outer ($R > R_{\rm bar}$) regions. The horizontal dotted lines denote $\lambda_z = 0.8$ and $\lambda_z = 0.25$, further classifying the orbits into cold ($\lambda_z \geq 0.8$), warm ($0.25 < \lambda_z < 0.8$), and hot ($\lambda_z \leq 0.25$) components. This results in six distinct components in total, with the luminosity fraction of each component labelled.

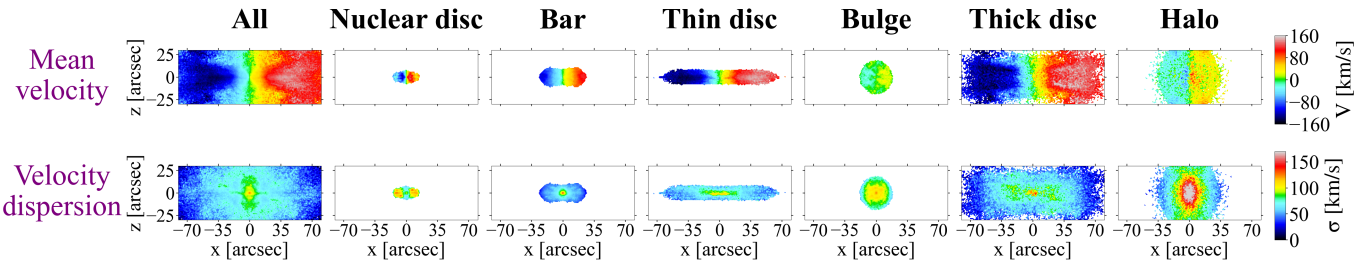


Fig. G.1. Spatial distributions of luminosity-weighted mean velocities (*top*) and velocity dispersions (*bottom*) on the *x*-*z* planes for dynamical components in the best-fitting model of NGC 1381. *From left to right*: Entire galaxy, nuclear disc, bar, thin disc, bulge, thick disc, and stellar halo. For each component, only pixels above specified brightness thresholds are plotted.

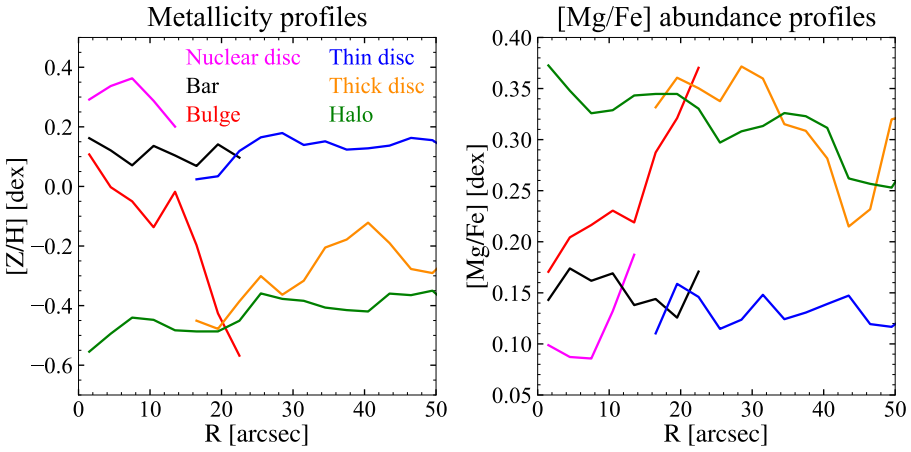


Fig. H.1. Stellar metallicity (*left*) and [Mg/Fe] abundance (*right*) profiles for the dynamical components in the best-fitting model of NGC 1381. The different colours represent different components: the nuclear disc (magenta), bar (black), bulge (red), thin disc (blue), thick disc (orange), and stellar halo (green).